University of Belgrade

Faculty of Physics

Master of Science

New Periodic Solutions to the Three-Body Problem and Gravitational Waves

Ana Hudomal

Thesis supervisor:

Dr. Veljko Dmitrašinović

Belgrade, October 2015

ACKNOWLEDGEMENTS

Most of all, I would like to express my gratitude to my thesis supervisor Veljko Dmitrašinović, who suggested the topic and helped me to develop a better understanding of the subject. He instructed me how to write a thesis, patiently corrected my writing, and was available whenever I needed help with this research.

I also owe my gratitude to Milovan Šuvakov, who developed the code that I used for calculations in this thesis and taught me how to use it, helped with technical details, and whose lecture inspired me to work on this topic in the first place.

I would like to thank Marija Janković for introducing me to Milovan Šuvakov and Veljko Dmitrašinović. She also helped me get familiar with M. Šuvakov's code, which she mastered first.

I would also like to thank the rest of my thesis committee, Marija Dimitrijević-Ćirić and Duško Latas for taking time to read my thesis.

I thank Miona Piperski for proofreading and correcting my English

Special thanks to my family and friends for supporting and encouraging me during the past year.

The computing cluster Zefram at the Institute of Physics in Zemun was used for most of the calculations in this thesis.

I acknowledge the financial support by the City of Belgrade studentship (Gradska stipendija grada Beograda) for the academic year 2012/2013, and the "Dositeja" stipend from the Fund for Young Talents of the Serbian Ministry for Youth and Sport for the academic years 2013/2014 and 2014/2015 (Fond za mlade talente - stipendija "Dositeja").

CONTENTS

1 INTRODUCTION

The Newtonian three-body problem is one of the oldest unsolved problems in physics and mathematics - it was first addressed in the 17th century by Newton himself, and latter by Euler, Lagrange, and many other scientists. The first big breakthrough was the discovery of periodic solutions by Euler and Lagrange in the 18th century, but there was very little progress during the next 200 years, except in the formal mathematical aspects in the 19th and early 20th century (Bruns, Poincaré, Sundman). Then in the second half of the 20th century the numerical approach began to develop with the advent of electronic computers, which resulted in the discovery of various new periodic three-body orbits.

In recent years, several new families of periodic solutions to the Newtonian three-body problem have been found at the Institute of Physics in Zemun. I first heard about that event from the local media, and soon after attended a lecture by Milovan Šuvakov on that topic at my University. This raised my interest in the three-body problem. In the spring of 2013 Marija Janković, my fellow student, asked me if I wanted to join the research on this topic with my present academic advisors, and I gladly accepted.

At that time I was still an undergraduate student, attending the second semester of the third year. After a few months of getting familiar with the basics, the real work started in the fall of 2013, when I was assigned to study gravitational waves emitted by the newly found three-body systems. In the spring of 2014 we had a paper ready for submission, and it was published later that summer, Ref. [1]. I presented a poster about our paper at the 2014 ICPS (International Conference of Physics Students) in Heidelberg. All of this happened before I started the Master's degree studies at the Faculty of Physics, University of Belgrade, so it was then only natural that I would continue working on these topics for the research part of my M.Sc. requirements.

The present thesis, submitted to the Faculty of Physics of University of Belgrade in partial fulfillment of the requirements for the degree of Master of Science, therefore contains some results that were obtained earlier.

As already stated above, some of the new orbits, which are the results of a continued search for periodic three-body orbits conducted over the past two years are presented in this thesis - 20 new orbits belonging to 18 families. This is not the total number of newly discovered orbits, however; only a few representative orbits from each sequence are shown here. Also, a new nomenclature convention for the orbits has been proposed.

Some properties of the newly discovered orbits were previously predicted, on the basis of recent empirical observations, but a few orbits presented a surprise. Even before this increase in the number of periodic orbits a topological method of classifying three-body orbits had been introduced, on purely formal grounds. Thus, a free group element, or a "word" for short, consisting of a sequence of letters $(\mathtt{a},\mathtt{b})$ and their inverses $(\mathtt{a}^{-1},\mathtt{b}^{-1}) = (\mathtt{A},\mathtt{B})$ is associated with each distinct topology.

These empirical observations indicate a linear dependence between the orbit's periods (rescaled to a common energy) and its "word length" – the number of "letters", or generators in the free group element that describes the orbit's topology. This property resembles Kepler's third law for periodic two-body systems. Several sequences of orbits have emerged, with slightly different slopes of this linear dependence. This observation can be used to predict the existence of further yet undiscovered periodic orbits.

The increase in the number of periodic orbits will certainly help the further study of their Kepler-like regularities, and of other properties as well, such as their emitted gravitational wave powers. With more available solutions, patterns in the free group elements of the orbits in the same sequence are becoming apparent. Some of the new results indicate that one of the previously defined sequences of orbits should actually be divided into (at least) three subsequences. All of this represents new contributions to our mathematical knowledge of the three-body problem.

The new solutions also lead to new astrophysical insights. A system of three massive bodies orbiting each other must emit gravitational waves. Actually, as shown in Ref. [1], astronomical triple-star systems can emit waves with greater amplitudes and thus luminosities than a periodic binary-star system with comparable masses and velocities, and at comparable distances. Despite having been predicted almost a century ago, gravitational waves have so far not been detected directly. Attempts to directly detect gravitational waves are ongoing – several gravitational wave observatories have been operating for more than 10 years, searching for any kind of gravitational radiation signal, albeit still without success.

The interest in studying gravitational radiation from the periodic three-body system has increased in recent years. The first such studies, about ten years ago (of periodic three-body orbits known at the time), did not find a significant increase in luminosities over those of binary systems. However, the luminosities of the periodic three-body systems discovered in the meantime turned out to be up to 13 orders-of-magnitude larger. Moreover, all of those new three-body orbits have distinct quadrupole gravitational waveforms.

I have now repeated the same type of calculations with the latest periodic systems, and the results are presented here. It turns out that the three-body orbits with luminosities of 10 orders-of-magnitude larger or more, than those of a two-body orbit are not rare at all: there are several such orbits even in this small sample. The quadrupole gravitational waveforms and instantaneous power graphs, despite being distinguishable in detail, show certain similarities in shape for the orbits that belong to the same sequence. These similarities could help to assign orbits to appropriate sequences.

2

THE THREE-BODY PROBLEM

How do three massive bodies move in the gravitational field of each other? This perhaps simple-sounding question has been the subject of extensive research of both physicists and mathematicians for almost two centuries after the discovery of Newton's gravitational law. A similar problem concerning two bodies is easily solvable; one can obtain the analytic form of their trajectories for any set of initial conditions. At the end of 19th century, Bruns finally demonstrated that the three-body problem does not have any new general integrals of motion in addition to the ten usual ones: the total energy, the linear and the angular momentum, Ref. [2].

What makes a three-body system so different from a two-body system? A system is said to be integrable if its number of degrees-of-freedom n equals the number of its involutive integrals-of-motion. Such systems can be reduced to quadrature (hence their name), which quadrature, in turn, can often be done in terms of analytic functions. But, integrable systems turn out to be the exception in Nature, rather than the rule. Unlike a two-body system, which has 6 (2x3) degrees-of-freedom in 3D space and 10 (1+3+3+3)[1] *nominal* integrals-of-motion; of the 10 only 7 (1+3+2+1)[2] are in involution. The Newtonian two-body problem is therefore (super)integrable. A three-body system, on the other hand has 9 (3x3) degrees-of-freedom and 7 (1+3+3) integrals-of-motion.[3]

As a result of this, the three-body problem cannot be solved in the same sense as the two-body problem; given arbitrary initial conditions it is not possible to obtain general closed-form solutions of Newton's equations governing the motion of the three bodies. The only exception is the Lagrange-Euler family of periodic orbits, which was found in the 18th century [4].

However, Bruns' result does not imply that other periodic orbits do not exist, only that they cannot be found systematically. In the 20th century, the advent of electronic computers has enabled another method of obtaining three-body problem periodic solutions - numerical simulations. Several new families of periodic collisionless three-body solutions have been discovered in this way. The first one was the Broucke-Hadjidemetriou-Hénon family in the 1970s, Refs. [5, 6, 7, 8, 9, 10, 11]. In the period 1993-2002 the second one followed, the Moore-Chenciner-Montgomery-Simó figure-eight family [12, 13]. The number of families was recently (2013) increased from three to fifteen, Ref. [14]. Each one of these families contains infinitely many different orbits with different angular momenta. New families of solutions that do not belong to the previously discovered ones continue to be found [15]. Several new families of orbits will be presented in this thesis.

1 energy + center-of-mass motion linear momentum + angular momentum + Lagrange-Runge-Lenz vector
2 See footnote 1.
3 M. Tabor, §2.5.b in Ref. [3] states: "... the key to integrating a Hamiltonian system of n degrees of freedom is to find *n independent integrals (constants) of motion*." and "A Hamiltonian system is said to be *completely integrable* if there exist n integrals of motion which are in *involution*."

2.1 EQUATIONS OF MOTION

In order to simplify the problem, we will first impose some restrictions on our system:

1. Only the non-relativistic three-body problem will be considered. The bodies move in the field of Newtonian gravity.
2. The three bodies are point masses, which means that the sizes of the bodies are negligible compared to the distances between them.
3. We will consider only planar three-body systems, where all bodies move in a fixed plane. The only requirement for this is that none of the bodies has a component of initial velocity perpendicular to the plane defined by their initial positions.

The position of the i-th body is described by its position vector $\mathbf{r}_i = (x_i, y_i)$. Masses are denoted by m_i, and the gravitational constant by G. A planar three-body system has 6 (3x2) degrees-of-freedom; evolution of the system is therefore described by six differential equations of motion. The first two are:

$$\begin{aligned}\ddot{x}_1(t) = &\frac{Gm_2\left(x_2(t)-x_1(t)\right)}{\left[\left(x_1(t)-x_2(t)\right)^2+\left(y_1(t)-y_2(t)\right)^2\right]^{3/2}}\\ &+\frac{Gm_3\left(x_3(t)-x_1(t)\right)}{\left[\left(x_1(t)-x_3(t)\right)^2+\left(y_1(t)-y_3(t)\right)^2\right]^{3/2}}\end{aligned} \tag{1}$$

$$\begin{aligned}\ddot{y}_1(t) = &\frac{Gm_2\left(y_2(t)-y_1(t)\right)}{\left[\left(x_1(t)-x_2(t)\right)^2+\left(y_1(t)-y_2(t)\right)^2\right]^{3/2}}\\ &+\frac{Gm_3\left(y_3(t)-y_1(t)\right)}{\left[\left(x_1(t)-x_3(t)\right)^2+\left(y_1(t)-y_3(t)\right)^2\right]^{3/2}},\end{aligned} \tag{2}$$

and the other four can be obtained by cyclic permutations $1 \to 2 \to 3 \to 1$. These equations have to be solved numerically. For a more detailed description of the method that I used, see Ref. [16].

The phase space of this system is 12-dimensional; the trajectory in the phase space is a 12-vector function of time t:

$$\mathbf{X}(t) = \left(\mathbf{r}_1(t), \mathbf{r}_2(t), \mathbf{r}_3(t), \dot{\mathbf{r}}_1(t), \dot{\mathbf{r}}_2(t), \dot{\mathbf{r}}_3(t)\right), \tag{3}$$

where $\dot{\mathbf{r}}_i(t)$ is the velocity of the i-th body. The initial conditions are specified by 12 numbers – components of the vector $\mathbf{X}_0 = \mathbf{X}(0)$.

2.2 THE RETURN PROXIMITY FUNCTION

A solution is absolutely periodic if the trajectory in the phase space returns to the initial point after some finite amount of time – period T: $\mathbf{X}(T) = \mathbf{X}_0$. We define the so-called return proximity function as[4]:

$$d(\mathbf{X}_0, T_0) = \min_{t<T_0} \|\mathbf{X}(t) - \mathbf{X}_0\|. \tag{4}$$

4 $\|\mathbf{X}(t)\| = \sqrt{\sum_{i=1}^{3} \mathbf{r}_i(t) + \sum_{i=1}^{3} \dot{\mathbf{r}}_i(t)}$ is the Euclidean norm.

The return proximity function measures the minimal distance to the initial point $\mathbf{X}_0$ reached during the time interval $[0, T_0]$. The condition for absolute periodicity with period $T < T_0$ is now equivalent to $d(\mathbf{X}_0, T_0) = 0$.

A solution is said to be relatively periodic if all relative positions and relative velocities of the three bodies return to their initial values after period T. All absolutely periodic solutions are also relatively periodic, and all relatively periodic solutions are absolutely periodic in some rotating coordinate system.

Various symmetries of the system can be used to simplify the return proximity function, and to make it suitable for searching for relatively periodic solutions. Translational symmetry can be used to set the total momentum to zero; this is done by changing the coordinate system so that the center-of-mass velocity is set to zero. For simplicity, the coordinate origin will be fixed at the center-of-mass.

$$\mathbf{R}_{CM} = \frac{m_1\mathbf{r}_1 + m_2\mathbf{r}_2 + m_3\mathbf{r}_3}{m_1 + m_2 + m_3} = 0 \tag{5}$$

$$\dot{\mathbf{R}}_{CM} = \frac{m_1\dot{\mathbf{r}}_1 + m_2\dot{\mathbf{r}}_2 + m_3\dot{\mathbf{r}}_3}{m_1 + m_2 + m_3} = 0 \tag{6}$$

In this way the phase space dimension, and thus the number of variables in the return proximity function is reduced to eight (by removing two coordinates and two velocities – four constants of motion).

To this point all the equations were written for the general case of bodies with arbitrary masses. From now on we will deal only with the systems of three bodies with equal masses m. The following procedure can be easily modified for different mass ratios.

2.3 JACOBI COORDINATES AND THE SHAPE-SPHERE

The graphical representation of the three-body system can be simplified with the use of rotational invariance – by changing the coordinates to the Jacobi ones [17]. Jacobi or relative coordinates are defined by two relative coordinate vectors:

$$\boldsymbol{\rho} = \frac{1}{\sqrt{2}}(\mathbf{r}_1 - \mathbf{r}_2), \qquad \boldsymbol{\lambda} = \frac{1}{\sqrt{6}}(\mathbf{r}_1 + \mathbf{r}_2 - 2\mathbf{r}_3). \tag{7}$$

These coordinates can now be used to define a new return proximity function:

$$d(\mathbf{Y}_0, T_0) = \min_{t<T_0} \|\mathbf{Y}(t) - \mathbf{Y}_0\|, \tag{8}$$

where $\mathbf{Y}$ is a 8-vector $\mathbf{Y}(t) = \big(\boldsymbol{\rho}(t), \boldsymbol{\lambda}(t), \dot{\boldsymbol{\rho}}(t), \dot{\boldsymbol{\lambda}}(t)\big)$ and $\mathbf{Y}_0 = \mathbf{Y}(0)$ contains the initial conditions. The zeros of this reduced return-proximity function correspond to absolutely periodic solutions.

Three independent scalar variables can be constructed from Jacobi coordinates: ρ^2, λ^2 and $\boldsymbol{\rho} \cdot \boldsymbol{\lambda}$. The overall size of the orbit is characterized by the hyperradius $R = \sqrt{\rho^2 + \lambda^2}$. These scalar variables are connected to the unit vector with Cartesian components:

$$\hat{\mathbf{n}} = \left(\frac{2\boldsymbol{\rho} \cdot \boldsymbol{\lambda}}{R^2}, \frac{\lambda^2 - \rho^2}{R^2}, \frac{2(\boldsymbol{\rho} \times \boldsymbol{\lambda}) \cdot \mathbf{e}_z}{R^2} \right). \tag{9}$$

Therefore, every configuration of three bodies (shape of the triangle formed by them, independent of size) can be represented by a point on a unit sphere. This sphere is called the shape-sphere.

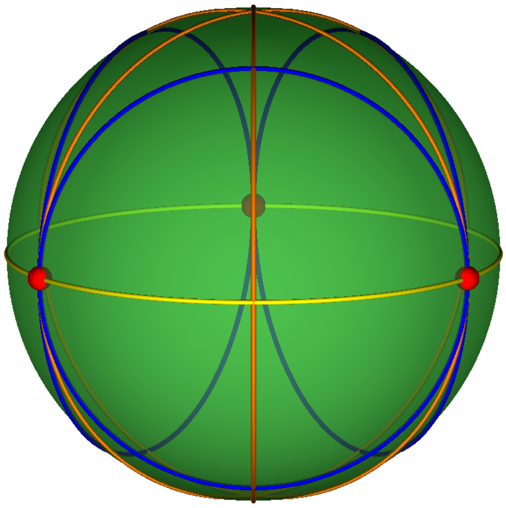

Figure 1: Shape-sphere with marked special configurations. Red: collision points. Yellow: equator. Orange: isosceles triangles. Blue: right-angled triangles.

The north and the south pole of the shape-sphere correspond to equilateral triangles which differ only in the orientation of bodies. In fact, a similar property holds for the whole northern and southern hemispheres; two triangles of the same shape but with opposite orientations are represented by two points that are symmetrical relative to the equatorial plane. The equator corresponds to degenerate triangles, where the bodies are in collinear configurations – syzygies. Three meridians at angles[5] $\varphi = -90°, 30°, 150°$ represent isosceles triangles. The intersection points of these meridians with the equator correspond to two-body collision points. Right-angled triangles are represented by points located on the three circles that contain exactly two collision points each. All other points on the shape-sphere represent triangles of general shape.

Every relatively periodic orbit of a three-body system is represented on the shape-sphere by a closed curve, or a point (Lagrange-Euler solutions). Two orbits with identical representations on the shape-sphere are considered to be the same solution. Since the shape-sphere coordinates do not depend on the overall size of the system, two orbits connected by scaling have identical curves on the shape-sphere. Orbits after symmetry trasformations are also considered to be the same solution as the original, although their representations on the shape-sphere can be different. Time-inversion does not change the trajectory on the shape-sphere, cyclic permutation of the bodies rotate the shape-space trajectory by $120°$ or $240°$ around the z-axis or reflect the trajectory across the equatorial plane, and the orbits that are mirror images of each other in real space correspond to trajectories that are also mirror images on the shape-sphere with mirror plane being the Euler plane[6].

The shape-sphere can be used to further reduce the number of variables in the return proximity function d to six: two angles that parametrize the sphere and the hyperradius R, together with their generalized momenta (time derivatives). Energy,

5 Azimuth φ is measured in counter-clockwise direction from $x = 0$. Cartesian coordinates are defined in eq. (9).

6 One Euler plane is defined by $\varphi = -90°$ – it contains both the Euler point and the coordinate origin, and is perpendicular to the equator. The Euler planes are equivalent to isosceles triangles.

or size scaling eliminates one of the variables, and thus brings their number down to five.

It has been demonstrated in Ref. [18] that every zero angular momentum solution to the Newtonian three-body problem passes through a collinear configuration (syzygy). This property allows us to choose a collinear initial configuration – a point on the equator of the shape-sphere. The space of initial conditions is in that case four-dimensional.

We can now define the relative return proximity function:

$$d(\mathbf{Z}_0, T_0) = \min_{t<T_0} \|\mathbf{Z}(t) - \mathbf{Z}_0\|, \tag{10}$$

where $\mathbf{Z}$ is a 6-vector $\mathbf{Z}(t) = (x, y, z, \dot{x}, \dot{y}, \dot{z})$, $\mathbf{Z}_0 = \mathbf{Z}(0)$ is the initial position vector, and

$$x = \frac{2\boldsymbol{\rho} \cdot \boldsymbol{\lambda}}{R}, \qquad y = \frac{\lambda^2 - \rho^2}{R}, \qquad z = \frac{2(\boldsymbol{\rho} \times \boldsymbol{\lambda}) \cdot \mathbf{e}_z}{R}. \tag{11}$$

Zeros of the relative return proximity function correspond to relatively periodic solutions.

2.4 CLASSIFICATION OF PERIODIC ORBITS

Periodic orbits can be classified according to the topology of their trajectories in the real configuration space ("braid group"), or on the so-called shape-sphere ("free group"), Refs. [14, 15, 16, 19]. The latter method of classification is used in this thesis.

Two-body collision points are singularities of the gravitational potential. A collisionless periodic orbit's trajectory on the shape sphere cannot pass through any of those points, nor can it be continuously stretched across them – collision points can therefore be considered punctures on the shape sphere.

A sphere with three punctures can be stereographically projected onto a plane with two punctures, by projecting one of the punctures on the sphere to infinity in the plane. In this way, the problem of classification is reduced to identifying topological classes of closed curves in a plane with two punctures. The fundamental group of such a plane is the free group on two elements $(\mathtt{a}, \mathtt{b})$. One clockwise turn around the first puncture is denoted by a, and similarly, one counterclockwise turn around the second puncture is denoted by b. The order of this group is infinite; its elements are products of an arbitrary number of a and b and their inverse elements, which will from now on be denoted by capitalized letters $\mathtt{a}^{-1} = \mathtt{A}$ and $\mathtt{b}^{-1} = \mathtt{B}$.

Each free group element (a sequence of a, b, A and B that forms a "word") is associated with one family of orbits. Since there is no preferred initial point of a periodic orbit, any cyclic permutation of the free group word corresponds to the same family. Cyclic permutations are obtained by series of conjugations; a family of orbits is therefore defined by the whole conjugacy class of a free group element.

A time-inversed orbit corresponds to a solution physically identical to the non-inversed one. Their free group elements are each other's inverse elements.

Permutations of the three-bodies also correspond to a physically identical solution. On the shape sphere, cyclic permutations are represented by rotations through 120° and 240° around the z-axis. A loop around the first puncture denoted by a after a cyclic permutation becomes a loop around the second puncture B, or a loop around the third puncture which is stereographically projected to infinity. A loop around infinity is equivalent to a loop around both punctures in the plane, which is denoted by `Ab`. Therefore `a`, `B` and `Ab` are equivalent.

An arbitrary number of neutral elements `aA` or `bB` can be added to a free group element; this is sometimes done in order to obtain a more compact form of the word – the one that contains powers of some simpler words. Because of this property, only the minimal number of letters in a free group element is well defined.

A review of previously known solutions:

1. Lagrange-Euler orbits – a single point on the shape sphere (neutral element `aA`)
   a) Lagrange's solutions (bodies remain in the configuration of an equilateral triangle) – north or south pole.
   b) Euler's solutions (bodies remain in a collinear configuration with one body exactly in the middle) – Euler's points (intersections of the equator and the symmetry meridians).

   Hyperangular degrees-of-freedom are frozen, all dynamics is reduced to hyperradial motions. The three-body problem is in this case solvable in general closed-form because of this property.

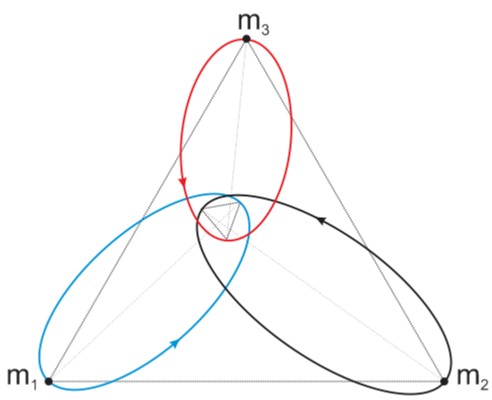

Figure 2: Lagrange's solution

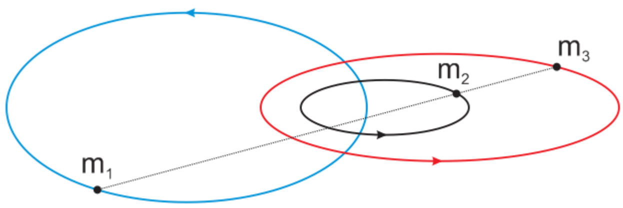

Figure 3: Euler's solution

2. Broucke-Hénon-Hadjidemetriou orbits – `a`

   Trajectories on the shape sphere of these solutions are ovals symmetrical relative to the equator and the meridian that passes through the collision point.

3. The figure-eight family – $(\texttt{abAB})^n$

   Moore's and Simó's figure-eight, and their satellites belong to this family. Moore's figure-eight is a choreography – an orbit such that all bodies move on exactly the same trajectory, only shifted in time by a third of the period. Satellites of the

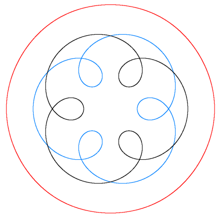

Figure 4: One of Broucke's solutions

order k of an orbit with free group word w are orbits with free group word w^k. See Figure 22 (Moore's and Simó's figure-eight are denoted by V.1.A and V.1.B, respectively).

4. Other – 12 new families, words with 8 letters and longer

   See Table 1 (taken from Ref. [14]). Two of the orbits belong to the same topological class – butterfly I and II. Orbits whose trajectories on the shape sphere pass trough the Euler's point twice have two different sets of initial velocities for collinear initial configurations (yin-yang I and II). They can be scaled and rotated into each other. Further classification and proposed nomenclature rules for new orbits will be explained in section 4.1.

2.5 NUMERICAL SEARCH FOR PERIODIC ORBITS

Equations of motion (1) and (2) need to be solved numerically. Many different methods of numerical integration exist, one of the most famous being the Runge-Kutta method. This method, with an adaptive time step, going by the name of the Runge-Kutta-Fehlberg method [20], was chosen for numerical calculations in this thesis, as implemented by Milovan Šuvakov in his code, Ref. [21]. An adaptive time step was chosen because some of the collisionless three-body orbits pass close to a two-body collision point (a singularity of the gravitational potential), where numerical error increases. In order to decrease this error, a shorter time step is needed. However, a short time step would unnecessarily increase integration time in regions far from the two-body collision points. This is why the time step needs to change according to the potential, so that the numerical error per step remains under some preset limit. The method that I used for numerical search is explained in more detail in Appendix 5.1.

2.6 OBSERVED KEPLER-LIKE REGULARITIES AMONG NEWLY FOUND PERIODIC ORBITS

Empirical observations indicate that the value of scaling invariant constant[7] $T|E|^{3/2}$ depends on the structure of the word $w(\mathtt{a}, \mathtt{b}, \mathtt{A}, \mathtt{B})$ that characterizes a periodic three-body orbit with zero-angular-momentum, Ref. [22]:

$$T(w)|E(w)|^{3/2} = \text{const}(w). \tag{12}$$

This property can be thought of as a three-body version of Kepler's third law.

7 Scaling laws: $\mathbf{r} \to \lambda \mathbf{r}$, $T \to \lambda^{3/2} T$, $E \to \lambda^{-1} E$.

Table 1: Initial conditions and periods of three-body orbits from Ref. [14]. $\dot{x}_1(0), \dot{y}_1(0)$ are the first particle's initial velocities in the x and y directions, respectively, T is the period. The other two particles' initial conditions are specified by these two parameters, as follows, $x_1(0) = -x_2(0) = -1$, $x_3(0) = 0$, $y_1(0) = y_2(0) = y_3(0) = 0$, $\dot{x}_2(0) = \dot{x}_1(0)$, $\dot{x}_3(0) = -2\dot{x}_1(0)$, $\dot{y}_2(0) = \dot{y}_1(0)$, $\dot{y}_3(0) = -2\dot{y}_1(0)$. The Newton's gravity coupling constant and equal masses are taken as $G = m_{1,2,3} = 1$.

Label	$\dot{x}_1(0)$	$\dot{y}_1(0)$	T	Free group element
butterfly I	0.30689	0.12551	6.2356	$(\mathtt{ab})^2(\mathtt{AB})^2$
butterfly II	0.39295	0.09758	7.0039	$(\mathtt{ab})^2(\mathtt{AB})^2$
bumblebee	0.18428	0.58719	63.5345	$(\mathtt{b}^2(\mathtt{ABab})^2\mathtt{A}^2(\mathtt{baBA})^2\mathtt{ba})$ $\times(\mathtt{B}^2(\mathtt{abAB})^2\mathtt{a}^2(\mathtt{BAba})^2\mathtt{BA})$
moth I	0.46444	0.39606	14.8939	$\mathtt{ba}(\mathtt{BAB})\mathtt{ab}(\mathtt{ABA})$
moth II	0.43917	0.45297	28.6703	$(\mathtt{abAB})^2\mathtt{A}(\mathtt{baBA})^2\mathtt{B}$
butterfly III	0.40592	0.23016	13.8658	$(\mathtt{ab})^2(\mathtt{ABA})(\mathtt{ba})^2(\mathtt{BAB})$
moth III	0.38344	0.37736	25.8406	$(\mathtt{babABA})^2\mathtt{a}(\mathtt{abaBAB})^2\mathtt{b}$
goggles	0.08330	0.12789	10.4668	$(\mathtt{ab})^2\mathtt{ABBA}(\mathtt{ba})^2\mathtt{BAAB}$
butterfly IV	0.350112	0.07934	79.4759	$((\mathtt{ab})^2(\mathtt{AB})^2)^6\mathtt{A}((\mathtt{ba})^2(\mathtt{BA})^2)^6\mathtt{B}$
dragonfly	0.08058	0.58884	21.2710	$(\mathtt{b}^2(\mathtt{ABabAB}))(\mathtt{a}^2(\mathtt{BAbaBA}))$
yarn	0.55906	0.34919	55.5018	$(\mathtt{babABabaBA})^3$
yin-yang I	0.51394	0.30474	17.3284	$(\mathtt{ab})^2(\mathtt{ABA})\mathtt{ba}(\mathtt{BAB})$
yin-yang I	0.28270	0.32721	10.9626	$(\mathtt{ab})^2(\mathtt{ABA})\mathtt{ba}(\mathtt{BAB})$
yin-yang II	0.41682	0.33033	55.7898	$(\mathtt{abaBAB})^3(\mathtt{abaBAbab})$ $\times(\mathtt{ABAbab})^3(\mathtt{AB})^2$
yin-yang II	0.41734	0.31310	54.2076	$(\mathtt{abaBAB})^3(\mathtt{abaBAbab})$ $\times(\mathtt{ABAbab})^3(\mathtt{AB})^2$

Moreover, this dependence is roughly linear: $T \simeq n + \bar{n}$, where $n = n_{\mathtt{a}} = n_{\mathtt{b}}$ and $\bar{n} = n_{\mathtt{A}} = n_{\mathtt{B}}$ are the numbers of letters a, b and A, B in the orbits' free group elements (compare columns $\mathrm{T}/\mathrm{T}_{\mathrm{M8}}$ and $(n+\bar{n})/2$ in Table 2).

Five sequences of orbits[8] were separated in Ref. [22]. Orbits within each of these sequences follow the linear rule more precisely, compare $\mathrm{T}/\mathrm{T}_\beta$ and $(n+\bar{n})/(n_\beta+\bar{n}_\beta)$ in Table 2.

The word that characterizes topology of the "II.B.1 yarn" solution is the third power of the time reversed word that describes the "I.B.1 moth I" orbit. Moth I and yarn orbits therefore form in a progenitor-satellite relationship with $k = 3$. The ratio of their periods equals three, to less than one par per thousand, as can be seen from Table 2. This was until now the only available data about satellites of orbits other than the figure-eight orbit.

2.6.1 *Predictions*

On the basis of these empirical regularities, Ref. [22] predicted:

1. new "yin-yang" orbits with ratios of periods $T/T(\text{II.C.2}) = k = 2, 3, 5, \ldots$;

8 Other than the figure-eight one.

Table 2: Taken from Ref. [22]. Periods T of three-body orbits rescaled to energy $E = -0.5$, their ratios with Moore's figure-8 period T_{M8}, and with period T_β of the first orbit β in the given section of the Table, as functions of the numbers $n_{\mathtt{a}}, n_{\mathtt{b}}, n_{\mathtt{A}}, n_{\mathtt{B}}$, of a's, b's, $\mathtt{A} = \mathtt{a}^{-1}$'s and $\mathtt{B} = \mathtt{b}^{-1}$'s respectively, in the free-group word description of the orbit. Different sequences of orbits are separated by horizontal lines.

Label	T	$\frac{T}{T_{M8}}$	$\frac{T}{T_\beta}$	$\frac{n+\bar{n}}{n_\beta+\bar{n}_\beta}$	$(n, \bar{n})$
M8	26.1281	1	1	1	1,1
S8	26.1268	0.999951	0.999951	1	1,1
I.B.1 moth I	68.4636	2.62031	1	1	2,3
II.B.1 yarn	205.469	7.86391	3.00114	3	6,9
I.A.1 butterfly I	56.3776	2.15774	1	1	2,2
I.A.2 butterfly II	56.3746	2.15762	0.999944	1	2,2
I.B.5 goggles	112.129	4.29152	1.9889	2	4,4
I.B.7 dragonfly	104.005	3.98059	1	1	4,4
I.A.3 bumblebee	286.192	10.9534	2.7517	11/4	11,11
II.C.2a yin-yang I	83.7273	3.20449	1	1	3,3
II.C.2b yin-yang I	83.7273	3.20449	1	1	3,3
II.C.3a yin-yang II	334.876	12.8167	3.9996	4	12,12
II.C.3b yin-yang II	334.873	12.8166	3.9996	4	12,12
I.B.1 moth I	68.4636	2.62031	1	1	2,3
I.B.3 butterfly III	98.4354	3.76742	1.43778	7/5	3,4
I.B.2 moth II	121.006	4.63126	1.76745	9/5	4,5
I.B.4 moth III	152.33	5.83013	2.22498	11/5	5,6
I.B.6 butterfly IV	690.627	26.4324	10.0875	49/5	24,25

2. new "butterfly I - goggles" orbits with ratios of periods $T/T(\text{I.A.1})$ equal to 3, 4, 5, ... ;
3. new "dragonfly - bumblebee" orbits with $T/T(\text{I.A.3}) = 5/4,\ 3/2,\ 7/4,\ \ldots$;
4. new "moth I,II,III - butterfly III" orbits with $n = 6,\ 7, \ldots$. The "butterfly IV" orbit deviates the most (8%) from this sequence, and may well define a sub-sequence of its own;
5. new satellites of "moth I", above and beyond the "yarn" orbit.

3

GRAVITATIONAL WAVES

Similarly to electromagnetic waves, which are emitted by accelerating particles with nonzero charge, accelerating massive particles emit gravitational waves. This result appears in both the special and the general theory of relativity. Unlike electromagnetic waves, where electric and magnetic fields oscillate in space and time, gravitational waves are actually oscillations in the curvature of space-time itself.

Gravitational radiation was first predicted by Einstein in 1916, soon after he had developed the theory of general relativity. Despite theoretical proof of their existence, gravitational waves have not yet been directly detected in an experiment. However, gravitational radiation has been detected indirectly. The binary system PSR1913+16 (consisting of a pulsar and another neutron star) which was discovered and studied by Hulse and Taylor loses energy and its period decreases at a rate consistent with the predictions of general relativity – the computed and observed rates agree to within the experimental accuracy, which is better than one percent [23]. Gravitational waves carry away energy and angular momentum, which causes the stars to spiral towards each other, to accelerate and to decrease their period. Hulse and Taylor were awarded the Nobel Prize in 1993 "for the discovery of a new type of pulsar, a discovery that has opened up new possibilities for the study of gravitation".

Aside from serving as another test of general relativity, direct detection of gravitational waves could bring about a breakthrough in astronomy. Efforts to directly detect gravitational waves are ongoing at several gravitational wave observatories operating around the world and they are constantly developing new detection technologies with better precision. The most advanced one, LIGO (Laser Interferometer Gravitational-Wave Observatory) was searching for waves emitted from binary coalescence from 2002 to 2010, but failed to detect any credible signal. A new experiment (aLIGO - Advanced LIGO) was supposed to start in September 2015. Several other detectors are operating around the world, such as VIRGO, GEO, TAMA and ACIGA. The ESA (European Space Agency) is planning to set up a gravitational wave observatory in space (eLISA – Evolved Laser Interferometer Space Antenna) – in 2034.

3.1 PROPAGATION OF GRAVITATIONAL WAVES

Derivation of gravitational waves in general relativity is explained in detail in Appendix 5.2.

A passing gravitational wave alternately stretches and compresses space in directions perpendicular to the direction of propagation of the wave – gravitational waves are therefore transverse waves. Gravitational waves have two independent modes of linear polarization, the so-called "plus" and "cross" modes. Their names come from the shape of the deformation a ring of test particles experiences under the influence of the wave, see Figures 5 and 6. The relative deformation is measured by the gravitational wave strain, $h_+(t)$ and $h_\times(t)$ for plus and cross mode respectively. The two linear polarization modes can be rotated into each other by the angle 45° around the z-axis (opposed to electromagnetic waves, where this angle is 90°).

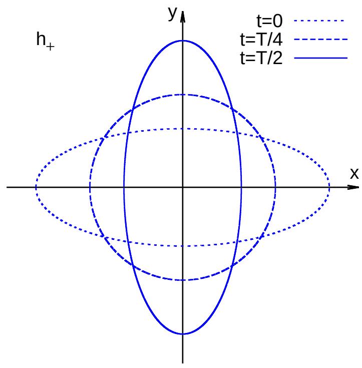

Figure 5: Plus polarization mode

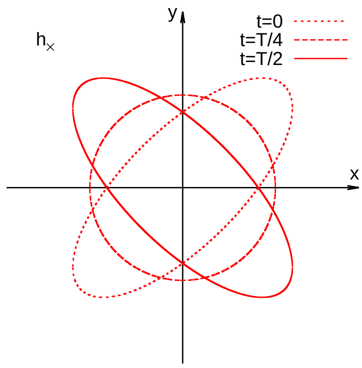

Figure 6: Cross polarization mode

The two independent modes of linear polarization are connected to the spin of the graviton – the hypothetical particle obtained after quantization of the gravitational field. Since the plus and cross polarization modes are invariant under the rotations of 180° around the z-axis, the graviton (in linearized general relativity) is expected to be a spin-2 particle. It also has to be massless, because gravitational waves propagate at the speed of light. A particle with the described properties has not been discovered so far, but it appears in all quantum theories of gravity.

Gravitational waveforms are graphs representing the change of h_+ and $h_\times$ over time. The shape of waveforms depends on the characteristics of the source's oscillations and position relative to the observer/detector.

3.2 GENERATION OF GRAVITATIONAL WAVES

All accelerating massive objects moving in spherically or cylindrically asymmetric ways are sources of gravitational waves. Possible astronomical sources include: two (or more) astronomical objects orbiting one another, binary coalescence (final merger of two compact binaries such as neutron stars or black holes), supernovae, rotating stars or planets (astronomical objects are never perfectly spherical), primordial gravitational radiation from the Big-Bang (gravitational analogue to the CMB).

The simplest form of gravitational radiation is quadrupole radiation, which differs from electromagnetic radiation where dipole is the simplest source. This difference arises from the fact that there are two types of electromagnetic charge – positive and negative, and only one type of gravitational charge – mass. In the same way that the law of charge conservation forbids monopole radiation in electromagnetism, monopole and dipole gravitational radiation are forbidden by the laws of mass and momentum conservation.

For a quadrupole gravitational wave, it can be shown (for a derivation of equations in this section see Refs. [24, 25]) that

$$h_{ij}^{TT} = \frac{2G}{rc^4}\frac{\mathrm{d}^2 Q_{ij}}{\mathrm{d}t^2} + \mathcal{O}\left(\frac{1}{r^2}\right), \tag{13}$$

where G is the gravitational constant, c the speed of light, r is the distance between the source and the observer, and

$$Q_{ij} = I_{ij} - \frac{1}{3}\delta_{ij}\sum_{k=1}^{3} I_{kk} \tag{14}$$

is the reduced quadrupole moment. This expression is known as the quadrupole formula. Quadrupole moment is defined as $I_{ij} = \int \rho x^i x^j \mathrm{d}V$, where $x^1, x^2, x^3 = x, y, z$ and $\rho(\mathbf{r}, t)$ is the mass density of the source. The reduced quadrupole moment equals zero in spherically or cylindrically symmetric systems, which explains why such systems do not emit gravitational radiation.

In this thesis, we are only interested in systems composed of three point-like bodies with equal masses m. Their mass density can be expressed using the delta-function $\rho = m\sum_{k=1}^{3}\delta(\mathbf{r}_k)$, in which case the quadrupole moment becomes $I_{ij} = m\sum_{k=1}^{3} x_k^i x_k^j$. The waveforms of a quadrupolar gravitational wave propagating along the z-axis now become:

$$h_+ = \frac{2Gm}{rc^4}\sum_{k=1}^{3}\left(\dot{x}_i^2 + x_i\ddot{x}_i - \dot{y}_i^2 - y_i\ddot{y}_i\right) \tag{15}$$

$$h_\times = \frac{2Gm}{rc^4}\sum_{k=1}^{3}\left(\ddot{x}_i y_i + 2\dot{x}_i\dot{y}_i + x_i\ddot{y}_i\right). \tag{16}$$

Instantaneous power energy loss of the radiating system per unit of time can be expressed as:

$$P = -\frac{\mathrm{d}E}{\mathrm{d}t} = \frac{G}{5c^5}\sum_{i,j=1}^{3} Q_{ij}^{(3)} Q_{ij}^{(3)}. \tag{17}$$

Luminosity of the system is defined as instantaneous power averaged over one period $\langle P \rangle$.

Units were set to $G = c = m = 1$ for all calculations throughout this thesis.

3.3 DETECTION OF GRAVITATIONAL WAVES

If a gravitational wave alternately stretches and compresses the space through which it is propagating (in the directions perpendicular to the direction of propagation), how should we detect its effects? For example, aren't the detection instruments also distorted together with space they sit in? This does not actually happen, because gravity is the weakest of all four fundamental interactions – this makes it negligible in comparison to the internal (atomic) forces that determine the shape of a solid object. A passing gravitational wave would change the dimensions of a solid object, but only by a negligible amount. A gravitational wave can cause free-standing (or free-hanging) objects such as a pendulum suspended in vacuum to move by a small but detectable amount. Such small displacements can be measured by optical interferometry with very high precision. This is the basis on which most contemporary gravitational wave detectors work. Another detection method relies on measuring the resonant oscillations of large metal cylinders.

The largest gravitational wave detector is LIGO - each of the two arms of its interferometer are 4km long [26]. LIGO actually consists of two identical detectors located on the "opposite" sides of the United States (in Livingston, Louisiana and Richland, Washington). A gravitational wave would have to be detected by both interferometers simultaneously in order to exclude external noise ranging from earthquakes and other seismic activity to even airplanes passing nearby [27].

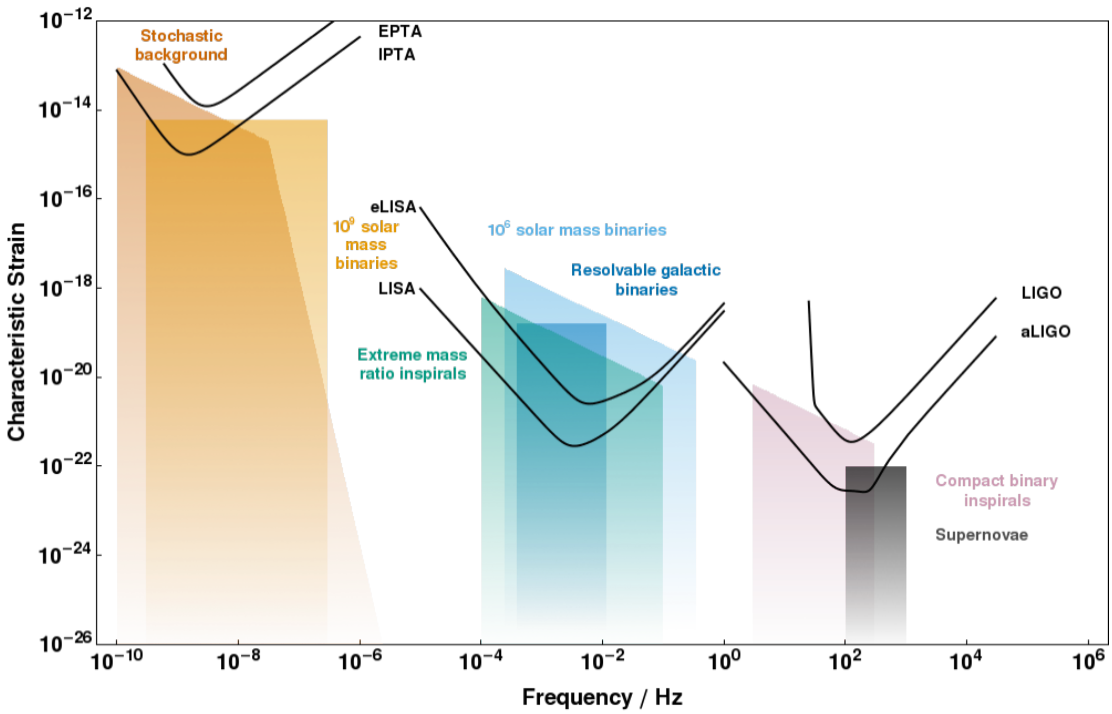

Figure 7: Detection windows – each gravitational wave observatory is best suited to detect waves from one type of sources – it can only detect waves whose frequencies are within a limited range and with amplitudes h above a certain threshold. Image taken from Ref. [28].

Because of its size, LIGO is able to detect displacements as small as 10^{-18}m [26]. For comparison, this is around a thousand times smaller then the size of a single proton. Displacements of that order of magnitude are predicted to be caused by gravitational waves emitted from, for example, binary coalescence of 10 solar mass black holes located outside our Galaxy. Binary coalescence is the only source for which there exists a precise prediction of the signal, see Refs. [29, 30, 31].

However, the problem with detection of this kind of waves is that the major part of energy emitted from binary coalescence comes from the final merger of two bodies. This event produces an intense burst of gravitational radiation which should be detected with current technology, but only if the detector is aiming at the right part of the sky in the right moment, because such events are never repeated in the same system. It is similar with supernovae, they are intense one-off events, but occur even more rarely than binary coalescence. Another problem with intense but rare events is that they are more likely to happen far away from Earth (their distribution in our Galaxy is poorly known), and the effects of gravitational waves emitted by them are greatly diminished before they reach the detectors.

On the other hand, (quasi)-periodic sources such as two-body orbits are not so rare and emit continual radiation, but they are weak sources of gravitational waves. As can be seen from the eq. (17), the power carried of by a quadrupolar gravitational wave is proportional to the square of the third time derivative of the reduced quadrupole moment, which is sensitive to the closest proximity to a two-body collision reached in a periodic orbit (close approach to a collision is accompanied by increases in velocities, accelerations and third derivatives of the relative positions which all increase the emitted power).

In the case of an isolated two-body system, a close approach to a collision inevitably leads to the actual collision and the destruction of that system. Getting as close as possible to a two-body collision but without the collision actually happening is therefore a desirable property of a radiating system whose gravitational waves are to be detected. The simplest systems of that kind are the three-body periodic orbits, where the gravitational influence of the third body can prevent a two-body collision even after a close approach. For this reason we shall study the gravitational waves emitted by known periodic three-body orbits, with some unexpected results.

4

RESULTS

In Ref. [14] a numerical search for periodic orbits was first done in the whole negative energy region - this is how the initial 13 orbits were found. Then in Ref. [15] Šuvakov "zoomed in" on a smaller window around the figure-eight orbit and found many satellites of the eight. This inspired us to make similar fine-comb searches around these 13 solutions. At first we took the window defined by $(p_1, p_2) \in [0.3, 0.5] \times [0.1, 0.5]$ with the resolution 2000×4000 (the return proximity function was computed for each point of the grid with step $s = 0.0001$). The maximal period was chosen to be $T_0 = 100$, same as in Ref. [14]. For comparison, the period of the Moore's figure-eight orbit is 6.325 in our units[1].

The search was later to extended to some other regions where we expected to find more solutions:

1. $[0.2, 0.3] \times [0.4, 0.5]$,
2. $[0.5, 0.6] \times [0.34, 0.46]$,
3. $[0.38, 0.44] \times [0.50, 0.54]$,
4. some smaller regions adjacent to the first search window and others around previously known orbits dragonfly $(p_1, p_2) = (0.0806, 0.5888)$ and bumblebee $(p_1, p_2) = (0.1843, 0.5872)$ [14].

Local minima with the return proximity function $< 10^{-2}$ were chosen as possible candidates for periodic solutions. There were around 200 such candidates. The gradient descent method with resolution $d_p = 0.0001$ was then performed for those candidate solutions, and the orbits with the resulting return proximity function $> 10^{-4}$ were excluded.[2]

4.1 NEW ORBITS

In order to classify the new periodic orbits, their free group elements ("words") had to be determined first. Most of these orbits have long words[3] that are practically impossible to be read directly from the shape sphere trajectory. Because of this, a computer program had to be used for this task. This code was also developed by Šuvakov, Ref. [21]. The free group word reading algorithm is described in Ref. [16].

The orbits were then divided into 5 sequences[4] that are defined in table 2 in section 2.6. They were first divided according to differences between their numbers n and $\bar{n}$,

1 $G = m = 1$
2 Some of the candidates with return proximity functions that are too large are probably connected to periodic solutions with slightly different initial conditions than (18).
3 The longest word has 110 letters.
4 One of these sequences was latter divided into 3 subsequences.

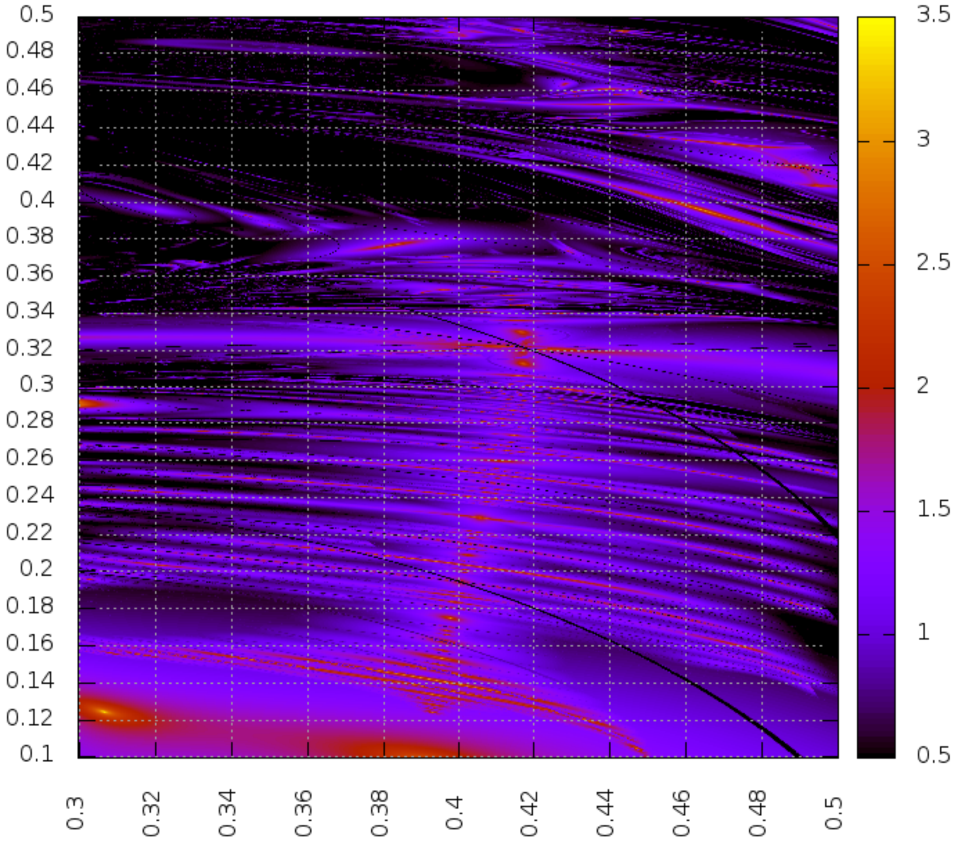

Figure 8: Negative decadic logarithm of the return proximity function for the region $[0.3, 0.5] \times [0.1, 0.5]$. Bright spots represent candidates for periodic orbits. Dark lines probably correspond to trajectories which lead to collision of two bodies.

and then placed into the sequence where they best fit (according to the slope of their linear dependece $T|E|^{3/2} \sim (n + \bar{n})$, explained in section 2.6). Only the first few orbits in each sequence (with shortest words) will be presented.

Because of their large number, a nomenclature system for periodic orbits has to be invented. New orbits will be named following the pattern S.n.X.α[5], where:

1. S is the sequence number (roman numeral)

2. n is the smaller of numbers n and $\bar{n}$ (if they are different)

3. X$\in$\{A,B,C,...\} denotes different orbits in case there are more then one with the same n in the same group

5 Not to be confused with orbit classes from Refs. [14] and [22]; that notation corresponds to geometric and algebraic symmetries of the orbits.

4. α or β denotes two different sets of initial conditions for the same solution if they exist at all.[6]

4.1.1 *Sequence I – butterfly I* (n, n)

Table 3: First few orbits in sequence I – butterfly I. Columns are the same as in Table 2 (except that the second one contains the invariant $T|E|^{3/2}$ instead of period T rescaled to energy $E = -0.5$). Old orbits are relabeled according to the new naming convention. New orbits are denoted by an asterisk.

Label	$\mathrm{T}\vert\mathrm{E}\vert^{3/2}\mathrm{T}$	$\frac{\mathrm{T}}{\mathrm{T_{M8}}}$	$\frac{\mathrm{T}}{\mathrm{T}_\beta}$	$\frac{n+\bar{n}}{n_\beta+\bar{n}_\beta}$	$(n, \bar{n})$	Old label
I.2.A	19.9325	2.15774	1	1	2,2	butterfly I
I.2.B	19.9313	2.15762	0.99994	1	2,2	butterfly II
I.5.A	49.6301	5.37257	2.48991	2.5	5,5	*
I.8.A	79.2555	8.57959	3.97619	4	8,8	*
I.12.A	119.241	12.9081	5.98224	6	12,12	*

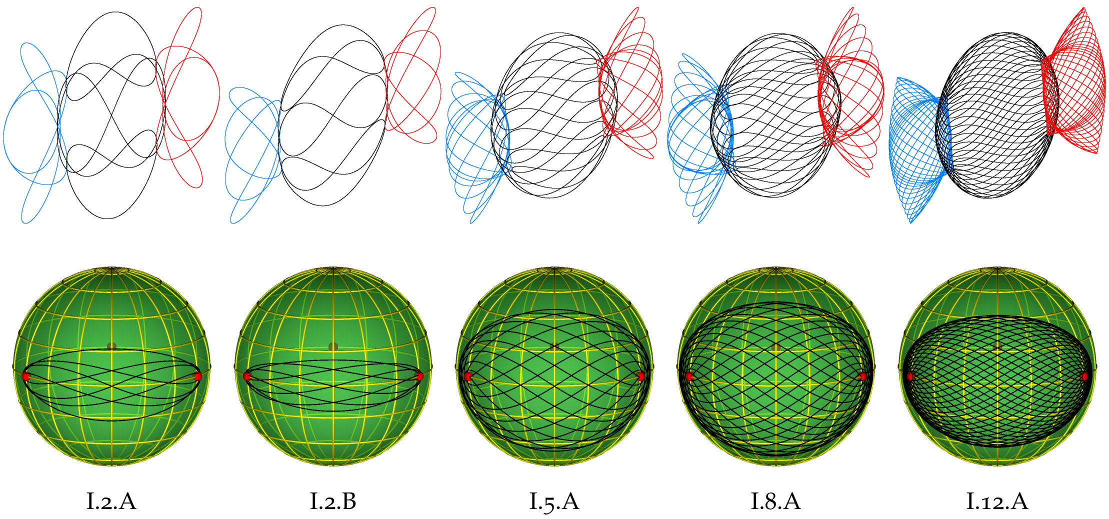

Figure 9: Top row: Real space trajectories of orbits from the butterfly I sequence (Table 3). Bottom row: Shape space trajectories of the same orbits.

These orbits have characteristic free group elements which contain sequences of letters $(\mathtt{ab})^2(\mathtt{AB})^2$ or $(\mathtt{ba})^2(\mathtt{BA})^2$ (see Table 4). All the orbits in this sequence have reflection symmetries around two axes – the equator and the meridian that passes through the Euler point. Orbits I.2.A, I.2.B, I.5.A and I.8.A also have algebraic exchange symmetries of free group elements $(\mathtt{a}, \mathtt{b}) \leftrightarrow (\mathtt{A}, \mathtt{B})$.

Orbits I.8.A with $\frac{T}{T_\beta} \approx 4$ and I.12.A with $\frac{T}{T_\beta} \approx 6$ were predicted in Ref. [22]. Orbit I.5.A was unexpected because it has an odd number $n = 5$, and all previously known orbits from this sequence had even numbers n.

6 This happens only when the orbit passes through the Euler point more than once – each passage can be taken for the initial configuration. Such orbits can be scaled into one another. Examples are the yin-yang a and b orbits from Ref. [14].

Linear fit $T|E|^{3/2} = a\left(\frac{n+\bar{n}}{2}\right) + b$ for all orbits from Table 3 gives $a = 9.924 \pm 0.015$ and $b = 0.04 \pm 0.11$ (see Figure 11).

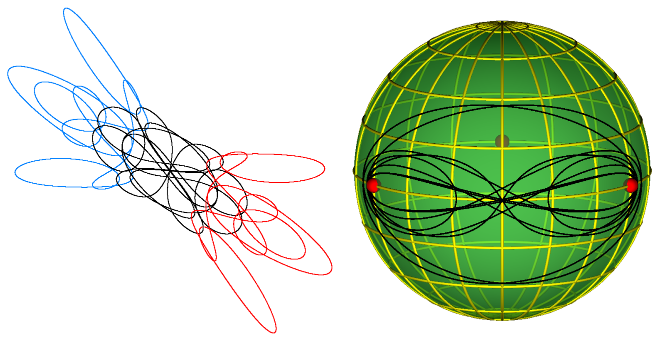

Figure 10: Goggles orbit. Left: real space. Right: shape-space.

The goggles orbit was also placed into this sequence in Ref. [22]. While it does fit in numerically, it looks completely different both in real space and on the shape-sphere (see Figure 10), and its free group element $(\mathtt{ab})^2\mathtt{ABBA}(\mathtt{ba})^2\mathtt{BAAB}$ does not contain $(\mathtt{ab})^2(\mathtt{AB})^2$ or $(\mathtt{ba})^2(\mathtt{BA})^2$. It was therefore excluded from this sequence.

Table 4: Free group elements of the orbits from Table 3 – sequence I.

Label	Free group element
I.2.A	$[(\mathtt{ab})^2(\mathtt{AB})^2]$
I.2.B	$[(\mathtt{ab})^2(\mathtt{AB})^2]$
I.5.A	$[(\mathtt{ab})^2(\mathtt{AB})^2]\mathtt{bA}[(\mathtt{ab})^2(\mathtt{AB})^2]\mathtt{B}[(\mathtt{ba})^2(\mathtt{BA})^2]\mathtt{a}$ $= (\mathtt{ab})^2(\mathtt{ABAbab})(\mathtt{AB})^2(\mathtt{abaBAB})$
I.8.A	$[(\mathtt{ab})^2(\mathtt{AB})^2]\mathtt{bA}^2[(\mathtt{ab})^2(\mathtt{AB})^2]\mathtt{B}[(\mathtt{ba})^2(\mathtt{BA})^2]\mathtt{aB}[(\mathtt{ba})^2(\mathtt{BA})^2]\mathtt{a}$ $= (\mathtt{AB})^2(\mathtt{abaBAB})^2(\mathtt{ab})^2(\mathtt{ABAbab})^2$
I.12.A	$[(\mathtt{ab})^2(\mathtt{AB})^2]\mathtt{b}[(\mathtt{ba})^2(\mathtt{BA})^2]\mathtt{aB}[(\mathtt{ba})^2(\mathtt{BA})^2]\mathtt{A}[(\mathtt{ab})^2(\mathtt{AB})^2]\mathtt{B}$ $\times[(\mathtt{ba})^2(\mathtt{BA})^2]\mathtt{A}[(\mathtt{ab})^2(\mathtt{AB})^2]\mathtt{b}[(\mathtt{ba})^2(\mathtt{BA})^2]\mathtt{a}$ $= [\mathtt{aba}(\mathtt{BA})^2\mathtt{bab}(\mathtt{AB})^2]^2(\mathtt{ba})^2(\mathtt{BA})^2[\mathtt{ABA}(\mathtt{ba})^2\mathtt{BAB}(\mathtt{ab})^2]^2$

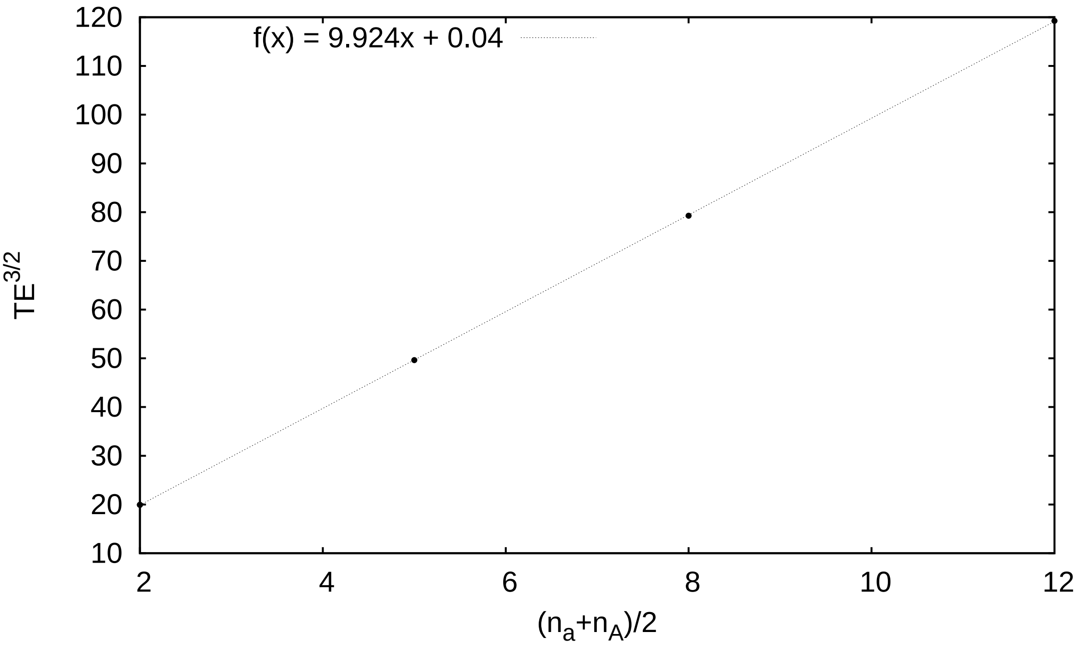

Figure 11: Linear fit of function $\mathrm{TE}^{3/2}(\frac{n+\bar{n}}{2})$ for butterfly I orbits from Table 3.

4.1.2 *Sequence II – dragonfly* (n, n)

Table 5: First few orbits in sequence II – dragonfly. Columns are the same as in Table 3.

Label	$\mathrm{TE}^{3/2}$	$\frac{\mathrm{T}}{\mathrm{T_{M8}}}$	$\frac{\mathrm{T}}{\mathrm{T}_\beta}$	$\frac{n+\bar{n}}{n_\beta+\bar{n}_\beta}$	$(n, \bar{n})$	Old label
II.4.A	36.7714	3.98059	1	1	4,4	dragonfly
II.6.A	55.2035	5.97591	1.50126	1.5	6,6	*
II.8.A	73.654	7.97321	2.00302	2	8,8	*
II.11.A	101.184	10.9534	2.75170	2.75	11,11	bumblebee

These orbits have characteristic free group elements with $\mathtt{A}^2$ and $\mathtt{B}^2$ followed by alternating sequences of letters ab and AB (see Table 6). Orbits II.4.A, II.6.A and II.11.A have reflection symmetries around two axes – the equator and the meridian that passes through the Euler point. Orbit II.8.A has central reflection symmetry around the Euler point. They also have algebraic exchange symmertries of free group elements; II.4.A and II.6.A $(\mathtt{a}, \mathtt{A}) \leftrightarrow (\mathtt{b}, \mathtt{B})$, and II.11.A $(\mathtt{a}, \mathtt{b}) \leftrightarrow (\mathtt{A}, \mathtt{B})$.

Orbits II.6.A with $\frac{T}{T_\beta} \approx \frac{3}{2}$ and II.8.A with $\frac{T}{T_\beta} \approx 2$ were predicted in Ref.[22].

Linear fit $T|E|^{3/2} = a\left(\frac{n+\bar{n}}{2}\right) + b$ for all orbits from Table 5 gives $a = 9.20 \pm 0.01$ and $b = -0.02 \pm 0.07$ (see Figure 13). This is the smallest slope value of all the sequences.

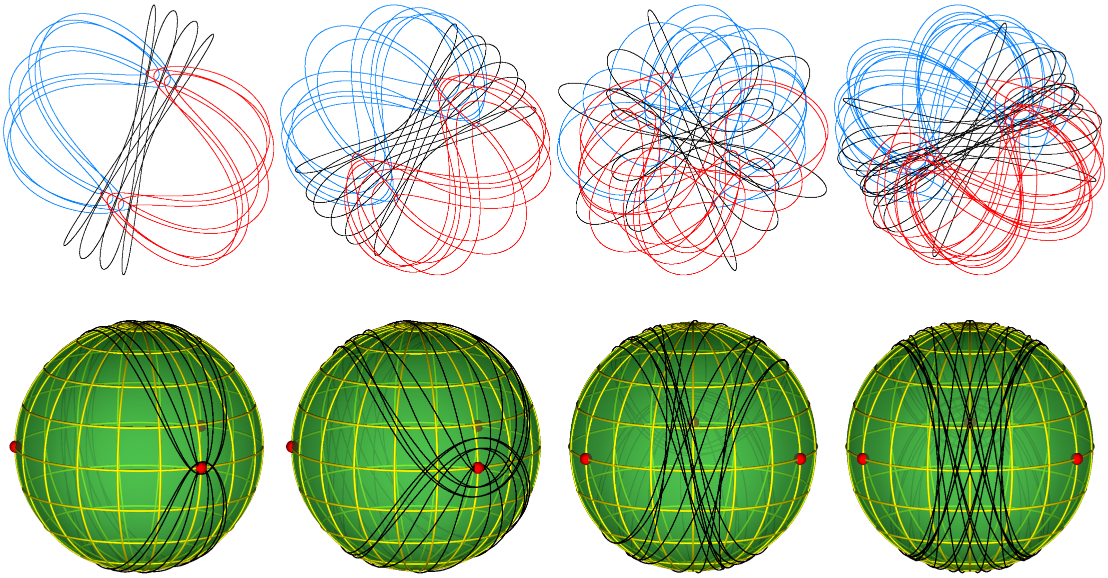

Figure 12: Top row: Real space trajectories of orbits from the dragonfly sequence (Table 5). Bottom row: Shape-space trajectories of the same orbits. Note how the shape-sphere trajectories of orbits II.4.A and II.6.A are rotated by $7\pi/6$, in order to show the trajectory around the third two-body collision point.

Table 6: Free group elements for the orbits from Table 5 – sequence II.

Label	Free group element
II.4.A	$\mathtt{a}^2(\mathtt{BAbaBA})\mathtt{b}^2(\mathtt{ABabAB}) = \mathtt{Ba}(\mathtt{BAba})^2\mathtt{Ab}(\mathtt{ABab})^2$
II.6.A	$\mathtt{A}^2(\mathtt{baBAbaBAba})\mathtt{B}^2(\mathtt{abABabABab}) = \mathtt{bA}(\mathtt{baBA})^3\mathtt{aB}(\mathtt{abAB})^3$
II.8.A	$\mathtt{A}^2(\mathtt{baBAbaBAbaBAbaBAba})\mathtt{B}^2(\mathtt{abABabABab}) = \mathtt{bA}(\mathtt{baBA})^5\mathtt{aB}(\mathtt{abAB})^3$
II.11.A	$[\mathtt{A}^2(\mathtt{baBAbaBAba})\mathtt{B}^2(\mathtt{abABabAB})][\mathtt{a}^2(\mathtt{BAbaBAbaBA})\mathtt{b}^2(\mathtt{ABabABab})]$ $= [\mathtt{bA}(\mathtt{baBA})^2\mathtt{aB}(\mathtt{abAB})^2][\mathtt{aB}(\mathtt{baBA})^3\mathtt{bA}(\mathtt{abAB})^3]$

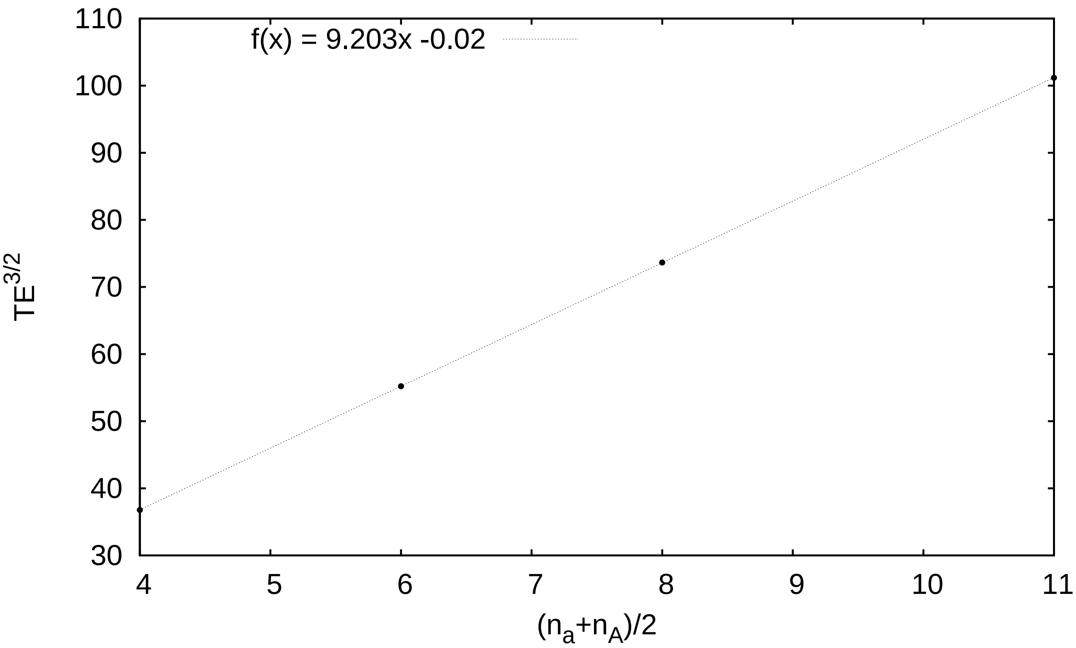

Figure 13: Linear fit of function $\mathrm{TE}^{3/2}(\frac{n+\bar{n}}{2})$ for dragonfly orbits from Table 5.

4.1.3 *Sequence III – yin-yang* (n, n)

Table 7: First few orbits in sequence III – yin-yang. Columns are the same as in Table 3.

Label	$TE^{3/2}$	$\frac{T}{T_{M8}}$	$\frac{T}{T_\beta}$	$\frac{n+\bar{n}}{n_\beta+\bar{n}_\beta}$	$(n, \bar{n})$	Old label
III.3.A	29.6021	3.20450	1	1	3,3	yin-yang Ia
III.9.A	88.8065	9.61351	3.000 007	3	9,9	*
III.12.A	118.396	12.8166	3.999 581	4	12,12	yin-yang IIa
III.15.A	147.998	16.0211	4.999 578	5	15,15	*

These orbits have characteristic free group elements that contain powers of `abaBAB` and `babABA` (see Table 8). Orbit III.9.A is a satellite of orbit I.3.A with $k = 3$. Its value of $T|E|^{3/2}$ is three times the value for the progenitor orbit, to the precision of $7 \cdot 10^{-6}$. This is a new satellite-progenitor pair of orbits, the first after the moth I - yarn pair and the figure-eight satellites.

All the orbits from this sequence have central reflection symmetry around the Euler point. They have no algebraic exchange symmetries of free group elements.

Orbits III.9.A with $\frac{T}{T_\beta} \approx 3$ and III.15.A with $\frac{T}{T_\beta} \approx 5$ were predicted in Ref. [22].

Linear fit $T|E|^{3/2} = a\left(\frac{n+\bar{n}}{2}\right) + b$ for all orbits from Table 7 gives $a = 9.8662 \pm 0.0004$ and $b = 0.005 \pm 0.004$ (see Figure 15).

Table 8: Free group elements for the orbits from Table 7 – sequence III.

Label	Free group element
III.3.A	$(\mathtt{abaBAB})\mathtt{a}(\mathtt{babABA})\mathtt{A}$
III.9.A	$[(\mathtt{abaBAB})\mathtt{a}(\mathtt{babABA})\mathtt{A}]^3$
III.12.A	$(\mathtt{abaBAB})^4\mathtt{b}(\mathtt{babABA})^4\mathtt{B}$
III.15.A	$(\mathtt{abaBAB})^5\mathtt{b}(\mathtt{babABA})^5\mathtt{B}$

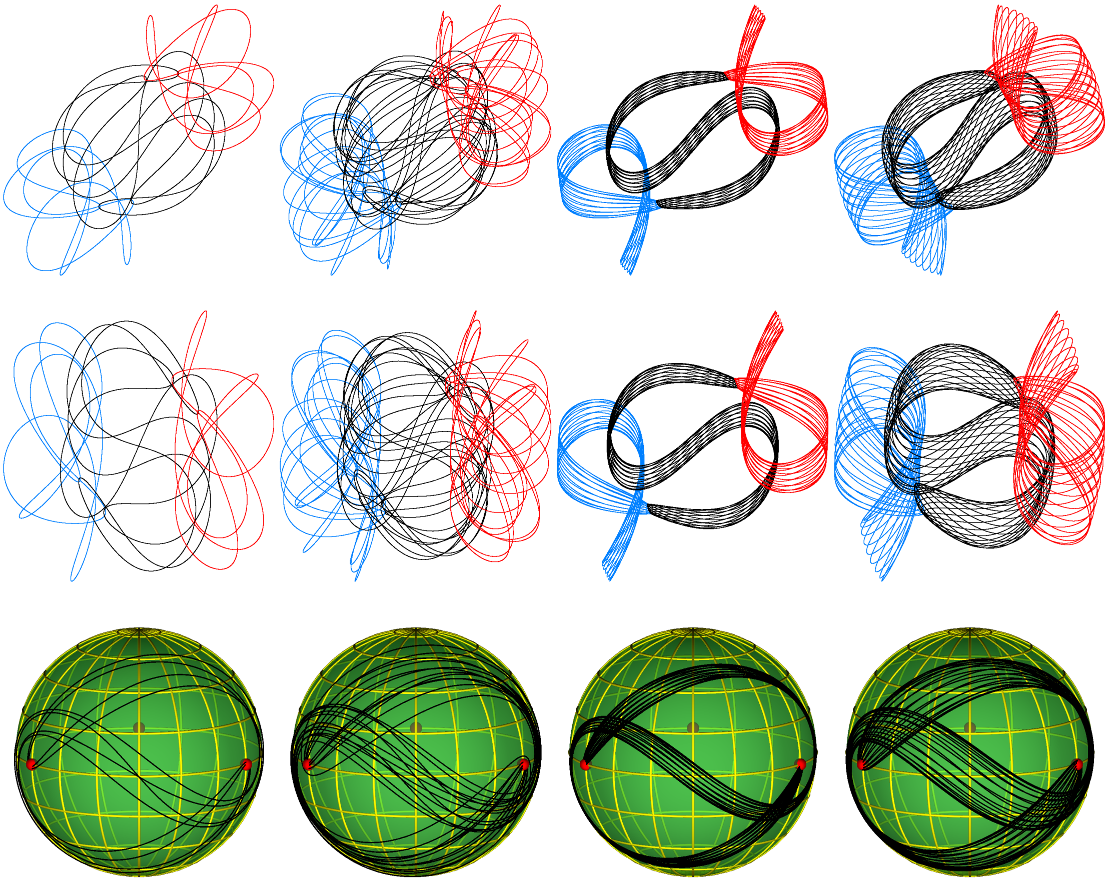

III.3.A III.9.A III.12.A III.15.A

Figure 14: Top row: Real space trajectories of α orbits from the yin-yang sequence (Table 7). Middle row: Real space trajectories of β orbits. Bottom row: Shape-space trajectories of the same orbits.

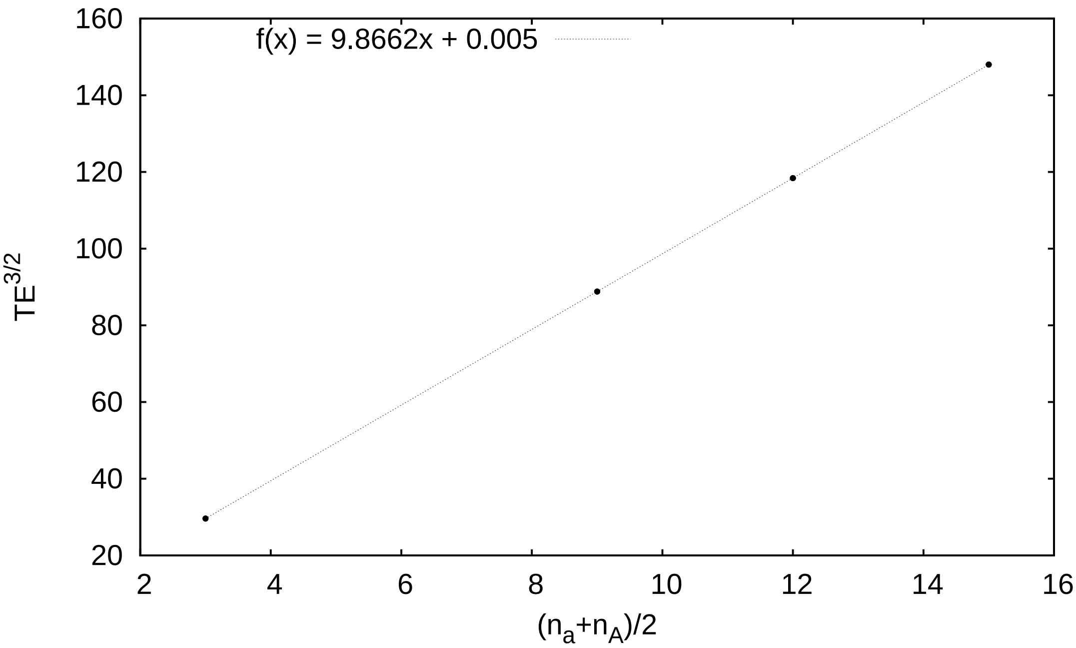

Figure 15: Linear fit of function $TE^{3/2}(\frac{n+\bar{n}}{2})$ for yin-yang orbits from Table 7.

4.1.4 *Sequence IVa – moth I* $(n, n+1)$

Table 9: First few orbits in sequence IVa - moth I.

Label	$TE^{3/2}$	$\frac{T}{T_{M8}}$	$\frac{T}{T_\beta}$	$\frac{n+\bar{n}}{n_\beta+\bar{n}_\beta}$	$(n, \bar{n})$	Old label
IVa.2.A	24.2056	2.62031	1	1	2,3	moth I
IVa.4.A	42.7821	4.63126	1.76745	1.8	4,5	moth II
IVa.6.A	61.2901	6.63479	2.53206	2.6	6,7	*
IVa.8.A	79.7794	8.63630	3.29591	3.4	8,9	*
IVa.8.B	79.7794	8.63630	3.29591	3.4	8,9	*
IVa.8.C	79.7794	8.63630	3.29591	3.4	8,9	*

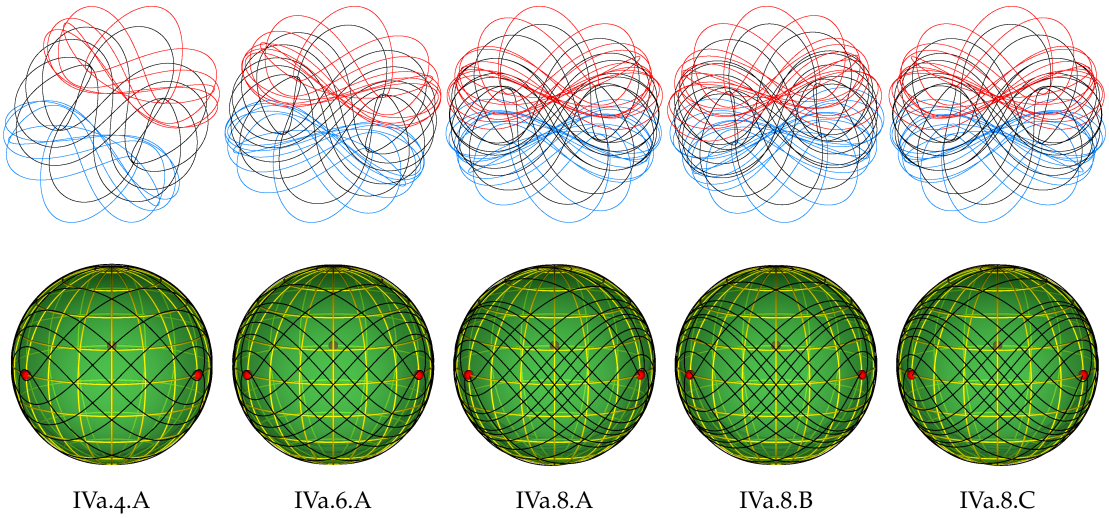

Figure 16: Top row: Real space trajectories of orbits from the moth I sequence (Table 9). Bottom row: Shape space trajectories of the same orbits.

This sequence and the following two (IVb and IVc) were a part of a larger sequence of orbits ("moth I, II, III - butterfly III") in Ref. [22]. Here they are divided into three parts, based on the slope of their $T|E|^{3/2}\left(\frac{n+\bar{n}}{2}\right)$ linear dependence, the appearance of their trajectories in real and shape-space, and the patterns in the words that define their topology.

These orbits have characteristic free group elements that contain powers of abAB and baBA (see Table 10). Orbits IVa.2.A, IVa.6.A and IVa.8.B have reflection symmetries around two axes – the equator and the meridian that passes through the Euler point. Orbits IVa.8.A and IVa.8.C have central reflection symmetry around the Euler point, and are mirror images of each other on the shape sphere. They have the same topology as the orbit IVa.8.B. All orbits have algebraic exchange symmetries of free group elements $(\mathtt{a}, \mathtt{A}) \leftrightarrow (\mathtt{b}, \mathtt{B})$.

Linear fit $T|E|^{3/2} = a\left(\frac{n+\bar{n}}{2}\right) + b$ for all orbits from Table 9 gives $a = 9.259 \pm 0.005$ and $b = 1.09 \pm 0.03$ (see Figure 17). Note the nonvanishing intercept b.

Table 10: Free group elements for the orbits from Table 9 – sequence IVa. Columns are the same as in Table 3.

Label	Free group element
IVa.2.A	$(\mathtt{abAB})\mathtt{A}(\mathtt{baBA})\mathtt{B}$
IVa.4.A	$(\mathtt{abAB})^2\mathtt{A}(\mathtt{baBA})^2\mathtt{B}$
IVa.6.A	$(\mathtt{abAB})^3\mathtt{A}(\mathtt{baBA})^3\mathtt{B}$
IVa.8.A	$(\mathtt{abAB})^4\mathtt{A}(\mathtt{baBA})^4\mathtt{B}$
IVa.8.B	$(\mathtt{abAB})^4\mathtt{A}(\mathtt{baBA})^4\mathtt{B}$
IVa.8.C	$(\mathtt{abAB})^4\mathtt{A}(\mathtt{baBA})^4\mathtt{B}$

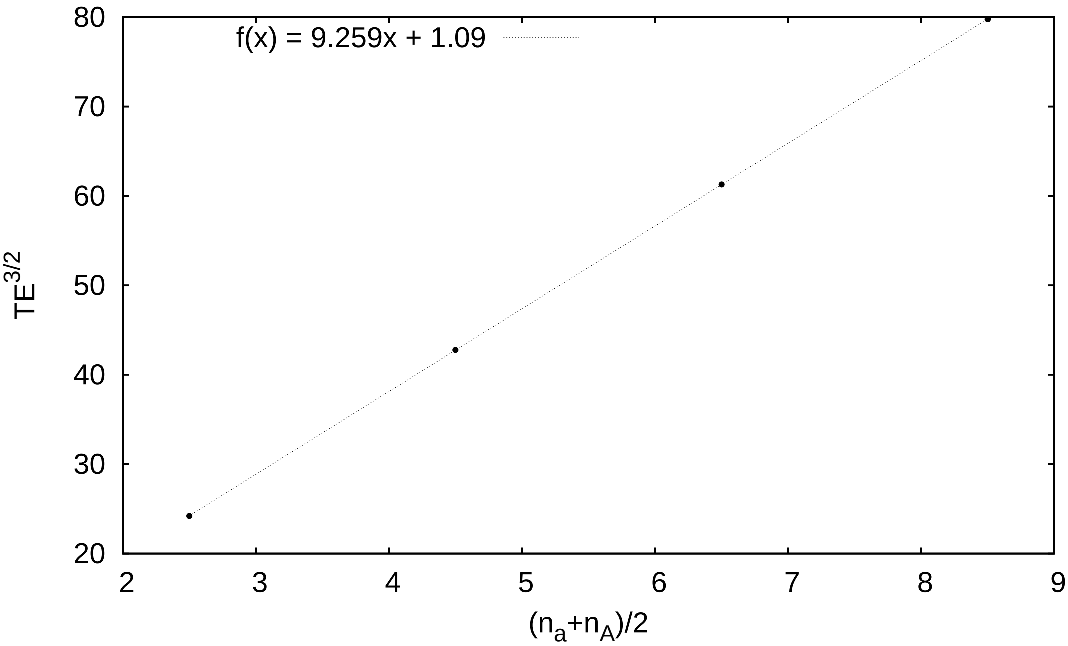

Figure 17: Linear fit of function $\mathrm{TE}^{3/2}(\frac{n+\bar{n}}{2})$ for moth I orbits from Table 9.

4.1.5 *Sequence IVb – butterfly III* $(n, n+1)$

These orbits have characteristic free group elements which contain sequences of letters $(\mathtt{ab})^2(\mathtt{AB})^2$ or $(\mathtt{ba})^2(\mathtt{BA})^2$ (see Table 12), same as the sequence I orbits. They are in fact very similar to the sequence I (butterfly I) orbits; the only difference is that in this case $\bar{n} = n + 1$ instead of $\bar{n} = n$.

All the orbits in this sequence have reflection symmetries around two axes – the equator and the meridian that passes through the Euler point. These orbits also have algebraic exchange symmetries of free group elements $(\mathtt{a}, \mathtt{b}) \leftrightarrow (\mathtt{A}, \mathtt{B})$.

Linear fit $T|E|^{3/2} = a\left(\frac{n+\bar{n}}{2}\right) + b$ for all orbits from Table 11 gives $a = 9.9695 \pm 0.0008$ and $b = -0.091 \pm 0.013$ (see Figure 19).

Table 11: Representative orbits from the sequence IVb – butterfly III. In this case several orbits with n ranging from 3 to 24 are presented instead of just the first few, because the previously known orbit – butterfly IV is one of the last ones.

Label	$TE^{3/2}$	$\frac{T}{T_{M8}}$	$\frac{T}{T_\beta}$	$\frac{n+\bar{n}}{n_\beta+\bar{n}_\beta}$	$(n, \bar{n})$	Old label
IVb.3.A	34.8022	3.7674	1	1	3,4	butterfly III
IVb.11.A	114.567	12.4021	3.29195	3.28571	11,12	*
IVb.15.A	154.433	16.7177	4.43745	4.42857	15,16	*
IVb.19.A	194.299	21.0333	5.58295	5.57143	19,20	*
IVb.24.A	244.172	26.4322	7.01599	7	24,25	butterfly IV

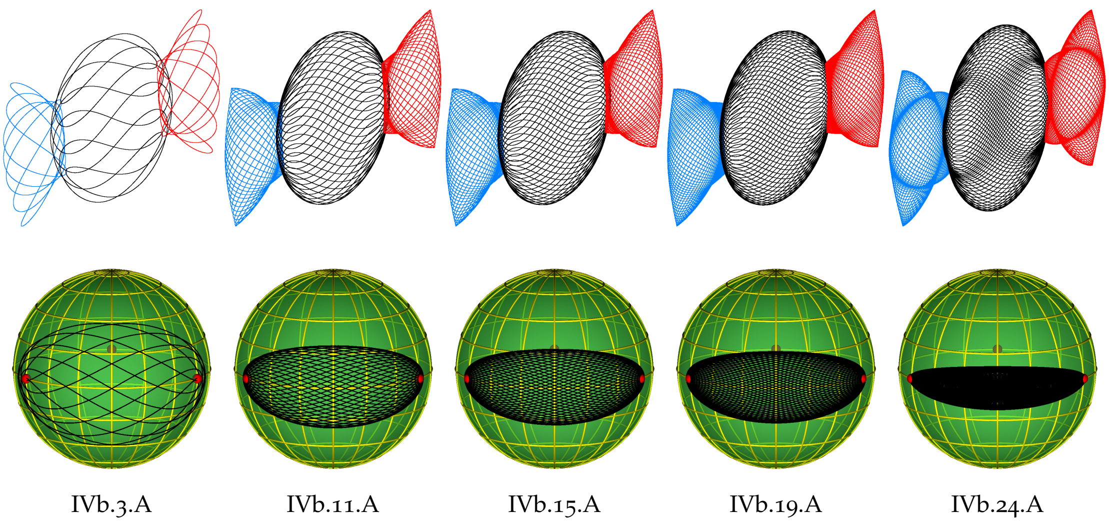

Figure 18: Top row: Real space trajectories of orbits from the butterfly III sequence (Table 11). Bottom row: Shape space trajectories of the same orbits.

Table 12: Free group elements for the orbits in Table 11 - sequence IVb.

Label	Free group element
IVb.3.A	$[(\mathtt{ab})^2(\mathtt{AB})^2]\mathtt{B}[(\mathtt{ba})^2(\mathtt{BA})^2]\mathtt{A}$
IVb.11.A	$[(\mathtt{ab})^2(\mathtt{AB})^2]^3\mathtt{a}[(\mathtt{ba})^2(\mathtt{BA})^2]^3\mathtt{b}$
IVb.15.A	$[(\mathtt{ab})^2(\mathtt{AB})^2]^4\mathtt{b}[(\mathtt{ba})^2(\mathtt{BA})^2]^4\mathtt{a}$
IVb.19.A	$[(\mathtt{ab})^2(\mathtt{AB})^2]^5\mathtt{b}[(\mathtt{ba})^2(\mathtt{BA})^2]^5\mathtt{a}$
IVb.24.A	$[(\mathtt{ab})^2(\mathtt{AB})^2]^6\mathtt{A}[(\mathtt{ba})^2(\mathtt{BA})^2]^6\mathtt{B}$

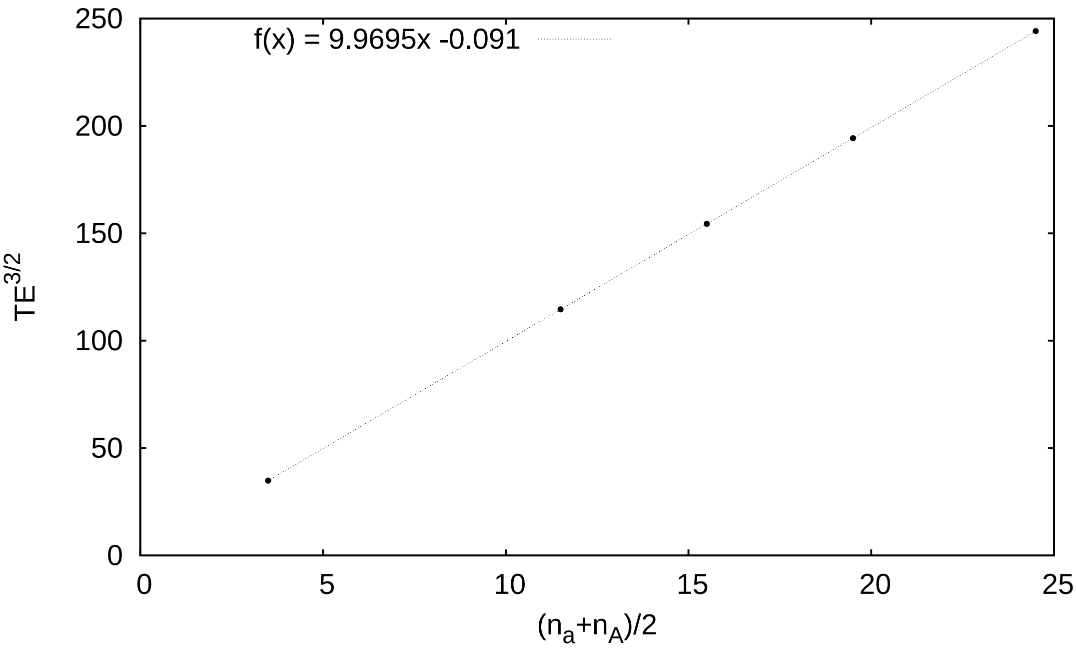

Figure 19: Linear fit of function $TE^{3/2}(\frac{n+\bar{n}}{2})$ for butterfly III orbits from Table 11.

4.1.6 *Sequence IVc – moth III* $(n, n+1)$

Table 13: First few orbits in sequence IVc – moth III.

Label	$TE^{3/2}$	$\frac{T}{T_{M8}}$	$\frac{T}{T_\beta}$	$\frac{n+\bar{n}}{n_\beta+\bar{n}_\beta}$	$(n, \bar{n})$	Old label
IVc.5.A	53.8569	5.83013	1	1	5,6	moth III
IVc.12.A.α	122.532	13.2644	2.27514	2.27273	12,13	*
IVc.12.A.β	122.532	13.2644	2.27514	2.27273	12,13	*
IVc.17.A	172.311	18.6531	3.19942	3.18182	17,18	*
IVc.19.A	191.207	20.6986	3.55028	3.54545	19,20	*

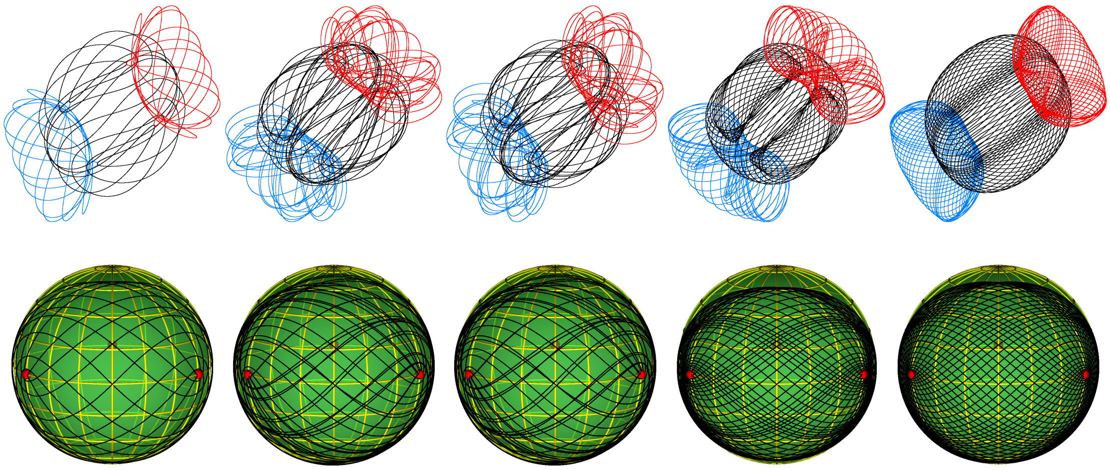

Figure 20: Top row: Real space trajectories of orbits from the moth III sequence (Table 13). Bottom row: Shape space trajectories of the same orbits.

These orbits have characteristic free group elements which contain the powers of letter sequences `abaBAB` and `babABA` (see Table 14), same as the yin-yang orbits.

Orbits IVc.5.A, IVc.17.A and IVc.19.A have reflection symmetries around two axes – the equator and the meridian that passes through the Euler point. Orbit IVc.12.A has central reflection symmetry around the Euler point. Orbits IV.5.A and IVc.17.A also have algebraic exchange symmetries of free group elements $(\mathtt{a}, \mathtt{A}) \leftrightarrow (\mathtt{b}, \mathtt{B})$.

Linear fit $T|E|^{3/2} = a\left(\frac{n+\bar{n}}{2}\right) + b$ for all orbits from Table 13 gives $a = 9.84 \pm 0.04$ and $b = -0.3 \pm 0.5$ (see Figure 13). The value of slope a agrees with the value for sequence III - yin-yang, within the stated absolute errors. This suggest that these two sequences may belong to one larger sequence, despite their different values of n and $\bar{n}$.

Table 14: Free group elements for the orbits from Table 13 – sequence IVc.

Label	Free group element
IVc.5.A	$[(\mathtt{babABA})^2\mathtt{a}(\mathtt{abaBAB})^2\mathtt{b}]$
IVc.12.A.α	$[(\mathtt{babABA})^3\mathtt{A}(\mathtt{abaBAB})^3\mathtt{B}][(\mathtt{babABA})^2\mathtt{a}(\mathtt{abaBAB})\mathtt{B}]$
IVc.12.A.β	$[(\mathtt{babABA})^3\mathtt{a}(\mathtt{abaBAB})^3\mathtt{b}][(\mathtt{babABA})\mathtt{A}(\mathtt{abaBAB})^2\mathtt{b}]$
IVc.17.A	$[(\mathtt{babABA})^6\mathtt{A}(\mathtt{abaBAB})^6\mathtt{B}]$
IVc.19.A	$[(\mathtt{babABA})^2\mathtt{a}(\mathtt{abaBAB})^2\mathtt{b}][(\mathtt{babABA})^3\mathtt{a}(\mathtt{abaBAB})^2\mathtt{b}]$ $\times[(\mathtt{babABA})^2\mathtt{A}(\mathtt{abaBAB})^3\mathtt{b}]$

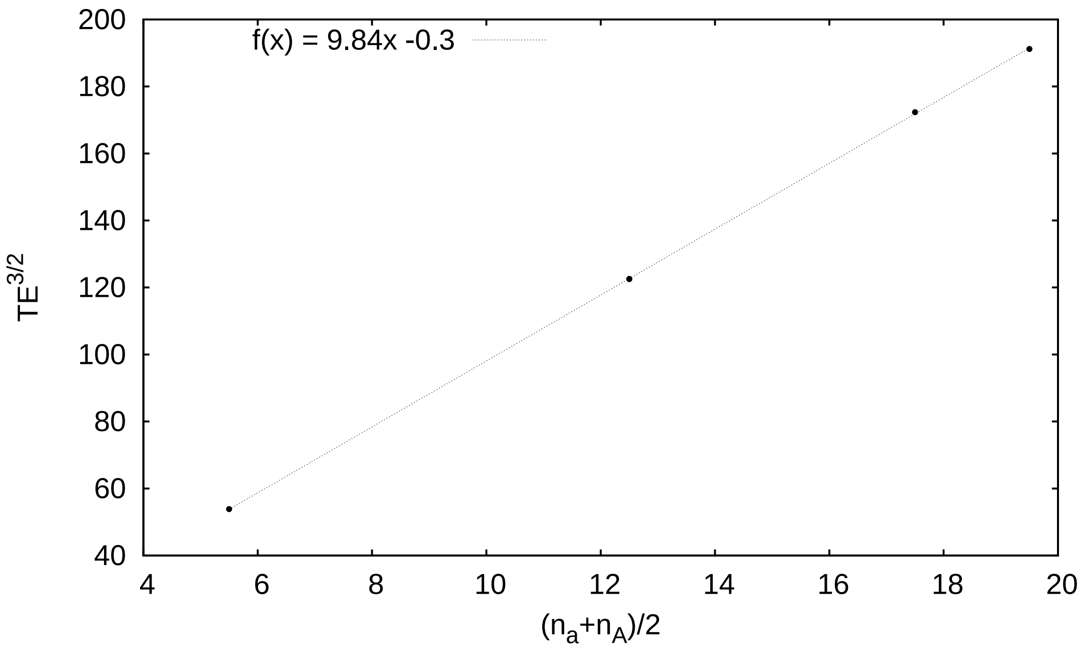

Figure 21: Linear fit of function $\mathrm{TE}^{3/2}(\frac{n+\bar{n}}{2})$ for moth III orbits from Table 13.

4.1.7 *Sequence V – figure-eight (n, n)*

All the oribits in the figure-eight family have free group words $(\mathtt{abAB})^k$, where $k = n$. Orbits V.1.A and V.1.B have reflection symmetries around two axes – the equator and the meridian that passes through the Euler point. Orbits V.4.A, V.15.A and V.20.A have central reflection symmetry around the Euler point. They also have algebraic exchange symmetries of free group elements $(\mathtt{a}, \mathtt{b}) \leftrightarrow (\mathtt{A}, \mathtt{B})$.

Linear fit $T|E|^{3/2} = a\left(\frac{n+\bar{n}}{2}\right) + b$ for all orbits from Table 15 gives $a = 9.2312 \pm 0.0015$ and $b = 0.003 \pm 0.017$ (see Figure 23).

Table 15: First few orbits in sequence V – figure-eight. In this case $T_{M8} = T_\beta$, so there is one less column in this table.

Label	$TE^{3/2}$	$\frac{T}{T_\beta}$	$\frac{n+\bar{n}}{n_\beta+\bar{n}_\beta}$	$(n, \bar{n})$	Old label
V.1.A	9.23768	1	1	1,1	M8
V.1.B	9.23721	0.99995	1	1,1	S8
V.4.A	36.9090	3.99548	4	4,4	*
V.15.A	138.503	14.9933	15	15,15	*
V.20.A	184.606	19.9840	20	20,20	*

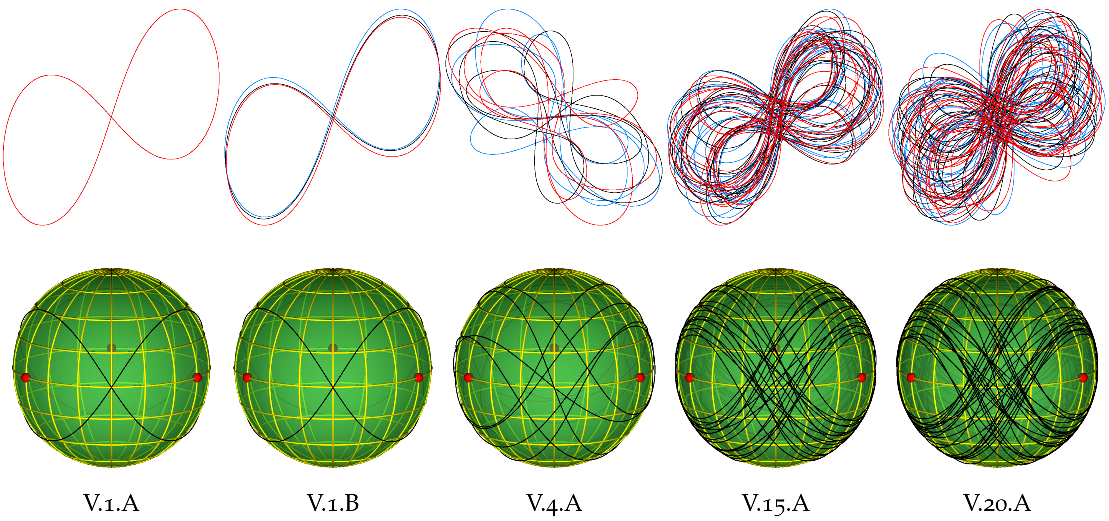

Figure 22: Top row: Real space trajectories of orbits from the figure-eight sequence (Table 15). Bottom row: Shape space trajectories of the same orbits.

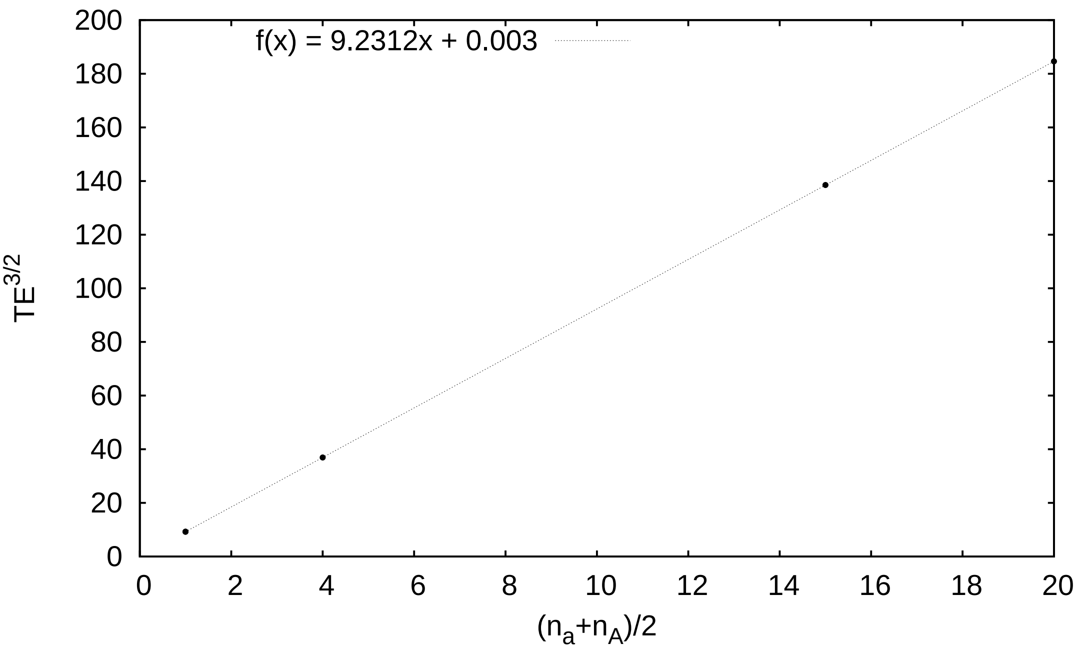

Figure 23: Linear fit of function $TE^{3/2}(\frac{n+\bar{n}}{2})$ for figure-eight orbits from Table 15.

4.2 WAVEFORMS AND LUMINOSITIES OF THE NEW THREE-BODY ORBITS

Gravitational waves from periodic three-body systems have already been studied in Refs. [32, 33, 34]. They have calculated the quadrupole radiation waveforms and luminosities for periodic orbits belonging to three families known at the time (Lagrange-Euler, figure-eight, Broucke-Hadjidemetriou-Hénon). However, the calculated luminosities were of the same order of magnitude as those from a comparable periodic two-body system.

This thesis is a continuation of work presented in Ref. [1]. Here we calculated the waveforms and luminosities for 13+11 recently discovered orbits (13 solutions belonging to 12 new families [14], and 11 new "satellite" orbits in the figure-eight family [21]). All the orbits were scaled to energy $E = -0.5$, in order to make a meaningful comparison between them. Units were set to $G = m = c = 1$. Orbits with two reflection symmetry axes were rotated in such a way that x and y coordinate axes coincide with symmetry axes. Orbits with a single point rotation symmetry are rotated so that the x and y axes are collinear with the eigenvectors of the moment-of-inertia tensor. In this way, a more symmetric shape of waveforms was obtained. These rotation angles are given in Tables 16-22.

Mean luminosities for these orbits range over 13 orders of magnitute, with maximal $1.23 \cdot 10^{13}$ for butterfly IV orbit (for comparison, Moore's figure-eight orbit has a mean luminosity of 1.35). Moreover, it turns out that orbits with large luminosities (over 10^{10}) are not a rarity, see figure 24. All of the orbits have distinguishable waveforms, whose number of peaks is proportional to the number of close approaches to a two-body collision point.

The quadrupole waveforms and instantaneous power graphs are symmetric under the reflection about time axis mid-point $T/2$ during one period T. This is a consenquence of the chosen initial conditions – all the orbits have vanishing angular momentum and pass through the Euler's point.

The same calculations are now repeated for new orbits from the previous section (4.1).

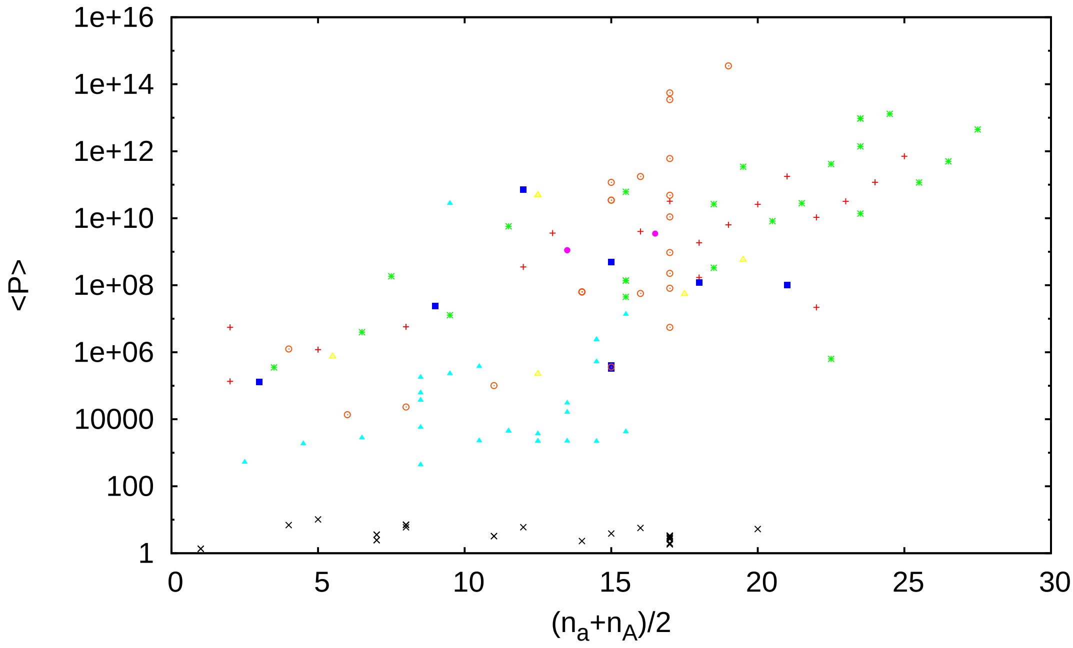

Figure 24: Luminosity averaged over one period (y-axis) as a function of $\frac{n+\bar{n}}{2}$ (x-axis). Note the logarithmic scale for luminosity. Orbits with luminosities of the order-of-magnitude $> 10^{10}$ are not a rarity. Black crosses: figure-eight. Blue triangles: moth I. Blue squares: yin-yang (n,n). Orange circles: dragonfly. Yellow triangles: moth III. Red pluses: butterfly I. Green stars: butterfly III. Pink circles: yin-yang (n,n+1).

4.2.1 *Sequence I – butterfly I* (n, n)

Orbits from the butterfly I sequence have luminosities that range from 10^5 to over 10^8, as can be seen in Table 16. Orbits I.2.A and I.2.B belong to the same topological class, but the latter has over 10 times larger luminosity because of its closer approach to a two-body collision point, see their shape-space trajectories in Figure 9.

Table 16: Initial conditions and periods of the orbits from sequence I – butterfly I. $\dot{x}_1(0), \dot{y}_1(0)$ are the first particle's initial velocities in the x and y directions, respectively, T is the period of the (rescaled) orbit to normalized energy $E = -1/2$, Θ is the rotation angle (in radians) and $\langle P \rangle$ is the mean luminosity (power) of the waves emitted during one period. The other two particles' initial conditions are specified by these two parameters, as follows: $x_1(0) = -x_2(0) = -\lambda$, $x_3(0) = 0$, $y_1(0) = y_2(0) = y_3(0) = 0$, $\dot{x}_2(0) = \dot{x}_1(0)$, $\dot{x}_3(0) = -2\dot{x}_1(0)$, $\dot{y}_2(0) = \dot{y}_1(0)$, $\dot{y}_3(0) = -2\dot{y}_1(0)$. The Newtonian coupling constant G is taken as $G = 1$ and the masses are equal $m_{1,2,3} = 1$.

Name	$\dot{x}_1(0)$	$\dot{y}_1(0)$	λ	T	Θ(rad)	$\langle P \rangle$
I.2.A	0.147 307	0.060 243	4.340 39	56.378	0.034 78	1.4×10^5
I.2.B	0.196 076	0.048 690	4.016 39	56.375	0.066 21	5.5×10^6
I.5.A	0.217 464	0.137 870	3.577 07	140.375	0.186 82	1.2×10^6
I.8.A	0.220 304	0.151 493	3.499 19	224.168	0.158 98	5.8×10^6
I.12.A	0.213 846	0.127 658	3.643 89	337.265	0.179 84	3.5×10^8

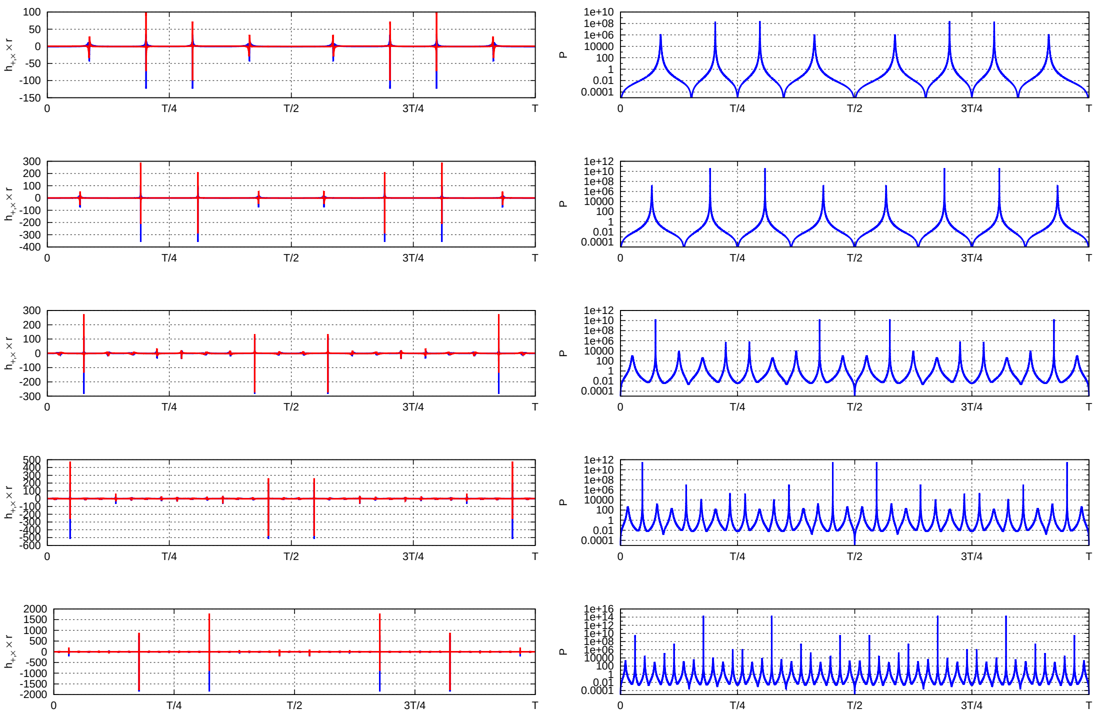

Figure 25: Left: Gravitational radiation quadrupolar waveforms $h_{+,\times} \times r$ for orbits from the butterfly I sequence (Table 16), where r is the radial distance from source to observer. Dotted blue curves denote the $+$ modes, and red solid curves $\times$ modes. Right: Instantaneous power of quadrupolar gravitational radiation as a function of elapsed time. Note the logarithmic scale for power. From top to bottom: I.2.A, I.2.B, I.5.A, I.8.A, I.12.A.

4.2.2 *Sequence II – dragonfly* (n, n)

Orbits from this sequence have luminiosities that range from 10^4 to over 10^6, see Table 17. Intrestingly, II.4.A, the orbit with the least n, has the largest luminosity. It would be expected that the luminosity is roughly proportional to n, because the orbits with larger n can approach the collision points more times in one period. Orbits with larger n indeed have more peaks in instantaneous emitted power, but closer approaches to the two-body collision points produce higher peaks (see Figure 26), which then result in greater overall luminosity. "Closeness to a collision point" can be seen from the orbits' trajectories on the shape-sphere, Figure 12.

Table 17: Orbits from sequence II – dragonfly. Columns are the same as in Table 16.

Name	$\dot{x}_1(0)$	$\dot{y}_1(0)$	λ	T	Θ(rad)	$\langle P \rangle$
II.4.A	0.047 479	0.346 935	2.880 67	104.005	-0.406 199	1.2×10^6
II.6.A	0.111 649	0.346 938	2.782 43	156.139	-0.820 428	1.4×10^4
II.8.A	0.082 172	0.308 060	3.105 75	208.325	1.273 42	2.3×10^4
II.11.A	0.111 581	0.355 545	2.727 51	286.192	-1.090 4	1.0×10^5

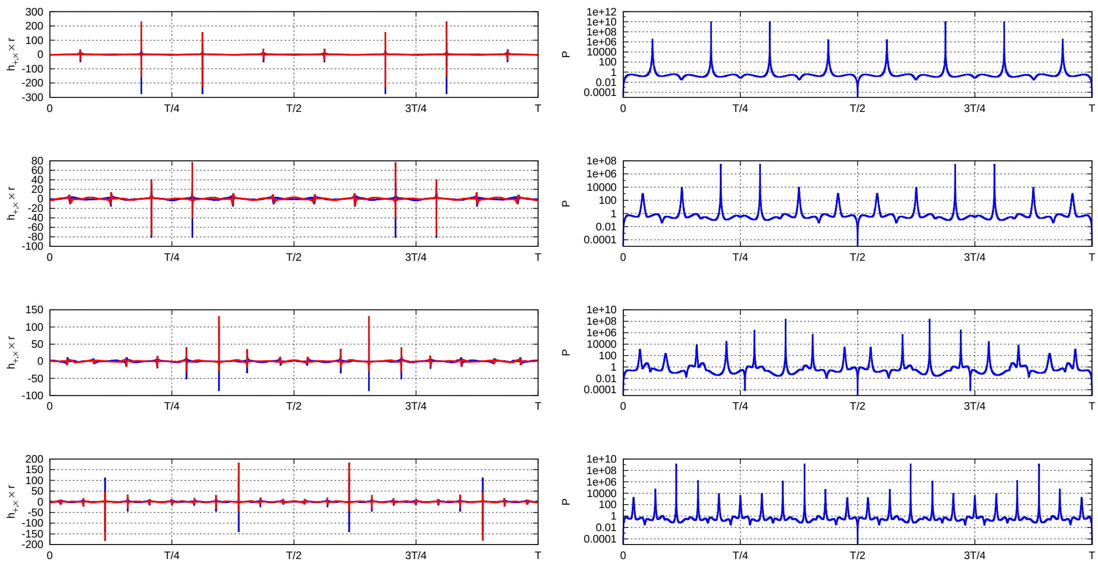

Figure 26: Same as in Figure 25 for orbits from the dragonfly sequence (Table 17). From top to bottom: II.4.A, II.6.A, II.8.A, II.11.A.

4.2.3 *Sequence III – yin-yang* (n, n)

Gravitational waveforms and instantaneous emitted power graphs are here shown only for one orbit from each pair. This is because the only difference between their graphs is that they are shifted in time for $T/2$, since these are the same orbits with different initial conditions. Obviously, they have exactly the same values of luminosities.

Same as with previous sequences of orbits, the orbit with the closest approach to the collision point, III.12.A (see Figure 14), has the largest luminosity $\langle \mathrm{P} \rangle \sim 10^{10}$.

Table 18: Orbits from sequence III – yin-yang. Columns are the same as in Table 16.

Name	$\dot{x}_1(0)$	$\dot{y}_1(0)$	λ	T	Θ(rad)	$\langle P \rangle$
III.3.A.α	0.304 003	0.180 257	2.858 02	83.727	0.659 242	1.3×10^5
III.3.A.β	0.143 554	0.166 156	3.878 10	83.727	-0.020 338	1.3×10^5
III.9.A.α	0.300 431	0.169 455	2.917 42	251.183	0.439 467	2.4×10^7
III.9.A.β	0.140 203	0.168 360	3.881 95	251.183	0.0513 222	2.4×10^7
III.12.A.α	0.229 355	0.181 764	3.302 84	334.877	0.472 891	7.2×10^{10}
III.12.A.β	0.227 451	0.170 639	3.366 76	334.872	0.254 995	7.2×10^{10}
III.15.A.α	0.228 839	0.187 327	3.279 22	418.601	0.649 370	5.0×10^8
III.15.A.β	0.226 509	0.164 556	3.400 64	418.601	0.091 698	5.0×10^8

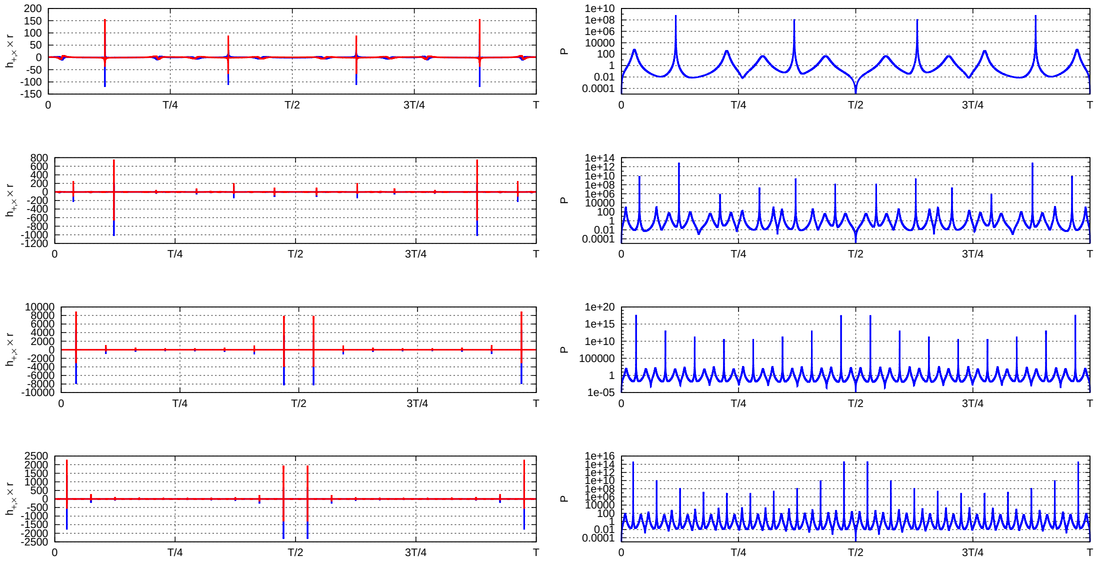

Figure 27: Same as in Figure 25 for orbits from the yin-yang sequence (Table 18). From top to bottom: III.3.A.α, III.9.A.α, III.12.A.α, III.15.A.α.

4.2.4 *Sequence IVa – moth I* $(n, n+1)$

The luminosities of orbits from the moth I sequence range from 10^2 to over 10^6. Orbits IVa.8.A and IVa.8.C have exactly the same values of luminosities, which is natural since they are mirror images of each other. Orbit IVa.8.B is in the same topological class as the previous two, but it has an order-of-magnitute smaller luminosity.

All the instantaneous power graphs have two large peaks in each half-period – these peaks correspond to the closest approaches to the two-body collision points that can be seen on their shape-space trajectories, Figure 16. These peaks are of the same height for orbits with reflectional symmetry (IVa.2.A, IVa.4.A, IVa.6.A and IVa.8.B).

Table 19: Orbits from sequence IVa – moth I. Columns are the same as in Table 16.

Name	$\dot{x}_1(0)$	$\dot{y}_1(0)$	λ	T	Θ(rad)	$\langle P \rangle$
IVa.2.A	0.279 332	0.238 203	2.764 56	68.464	0.899 49	5.2×10^{2}
IVa.4.A	0.271 747	0.280 288	2.611 72	121.006	1.138 78	1.9×10^{3}
IVa.6.A	0.281 803	0.289 097	2.527 88	389.211	1.257 33	2.4×10^{6}
IVa.8.A	0.249 451	0.304 409	2.591 55	225.650	-1.557 74	3.7×10^{4}
IVa.8.B	0.245 798	0.305 159	2.602 50	225.650	-1.474 43	5.8×10^{3}
IVa.8.C	0.253 073	0.307 580	2.561 60	225.650	1.559 48	3.7×10^{4}

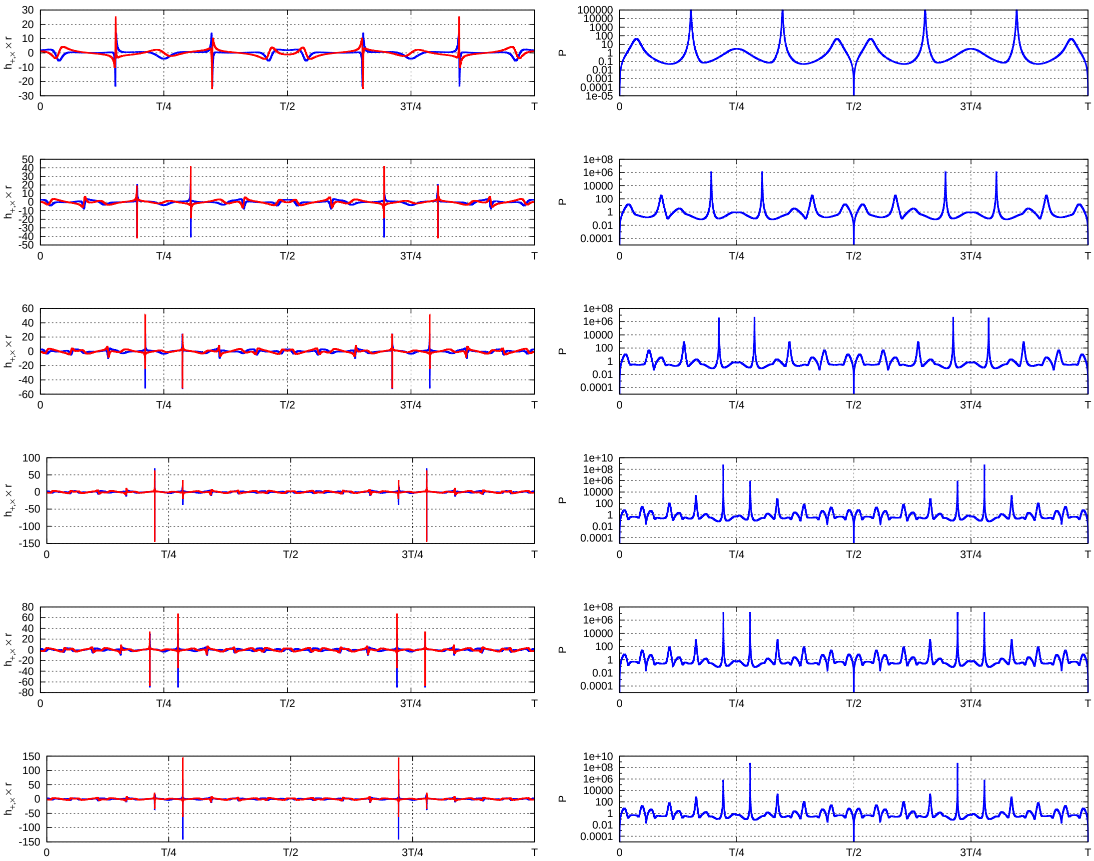

Figure 28: Same as in Figure 25 for orbits from the moth I sequence (Table 19). From top to bottom: IVa.2.A, IVa.4.A, IVa.6.A, IVa.8.A, IVa.8.B, IVa.8.C.

4.2.5 *Sequence IVb – butterfly III* $(n, n+1)$

Table 20: Orbits from sequence IVb – butterfly III. Columns are the same as in Table 16.

Name	$\dot{x}_1(0)$	$\dot{y}_1(0)$	λ	T	Θ(rad)	$\langle P \rangle$
IVb.3.A	0.211 210	0.119 761	3.693 54	98.435	0.170 326	3.5×10^{5}
IVb.11.A	0.199 886	0.078 032	3.917 70	324.043	0.107 860	5.8×10^{9}
IVb.15.A	0.199 062	0.071 624	3.941 56	436.804	0.098 823	6.2×10^{10}
IVb.19.A	0.197 960	0.067 703	3.959 99	549.561	0.092 685	3.5×10^{11}
IVb.24.A	0.170 296	0.038 591	4.226 76	690.632	0.038 484	1.2×10^{13}

Orbits from this sequence have the largest values of luminosities. Orbit IVb.24.A (previous name butterfly IV) has the maximum of all the orbits presented in this thesis. This is a consequence of their close approaches to the two-body collision points (as can be seen from their shape-space trajectories, Figure 18), and the large number of these approaches per one period. Each peak on the instantaneous power graph corresponds to one such close approach.

Instantaneous power graphs of these orbits resemble in shape the graphs of orbits from the butterfly I sequence.

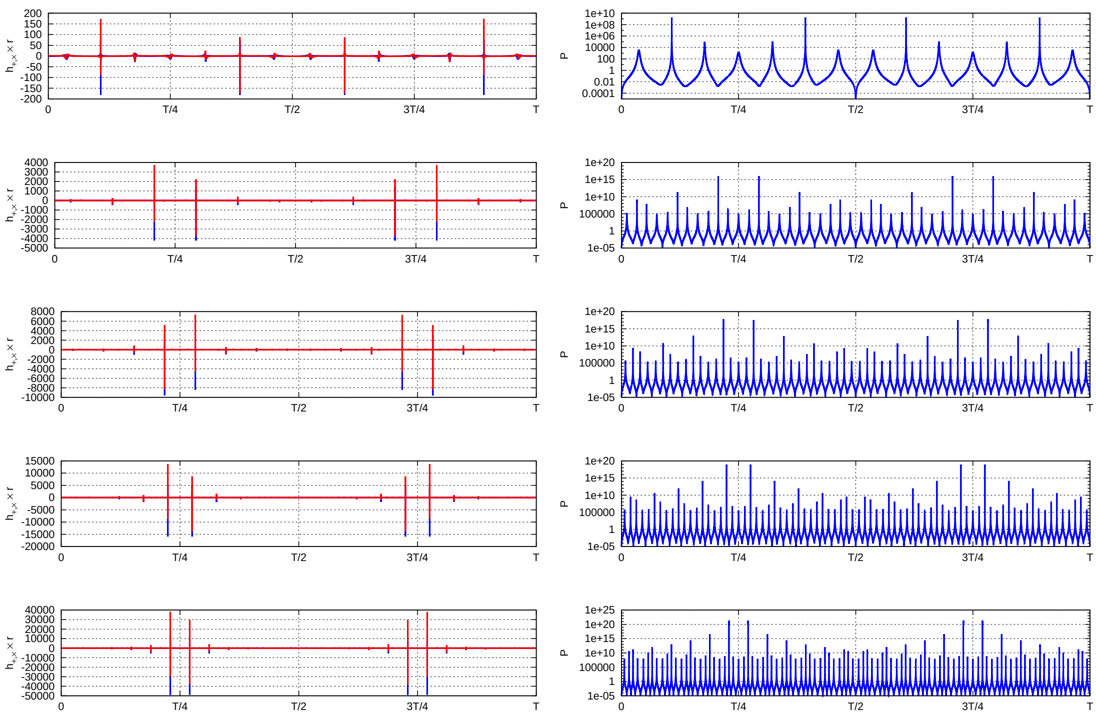

Figure 29: Same as in Figure 25 for orbits from the butterfly III sequence (Table 20). From top to bottom: IVb.3.A, IVb.11.A, IVb.15.A, IVb.19.A, IVb.24.A.

4.2.6 *Sequence IVc – moth III* $(n, n+1)$

Orbits from the moth III sequence have luminosities that range from 10^5 to over 10^{10}, see Table 21. The pair of orbits IVc.12.A has the maximal value of luminosity. Instantaneous power graphs of these orbits resemble in shape the graphs of orbits from the yin-yang sequence.

Table 21: Orbits from sequence IVc – moth III. Columns are the same as in Table 16.

Name	$\dot{x}_1(0)$	$\dot{y}_1(0)$	λ	T	Θ(rad)	$\langle P \rangle$
IVc.5.A	0.212 259	0.208 893	3.263 41	152.330	0.503 046	7.5×10^5
IVc.12.A.α	0.270 360	0.208 326	2.942 97	346.573	0.892 039	4.9×10^{10}
IVc.12.A.β	0.245 584	0.213 792	3.056 00	346.573	0.611 963	4.9×10^{10}
IVc.17.A	0.229 301	0.191 071	3.258 34	487.369	0.805 592	5.5×10^7
IVc.19.A	0.225 288	0.204 264	3.215 70	540.815	0.569 695	5.8×10^8

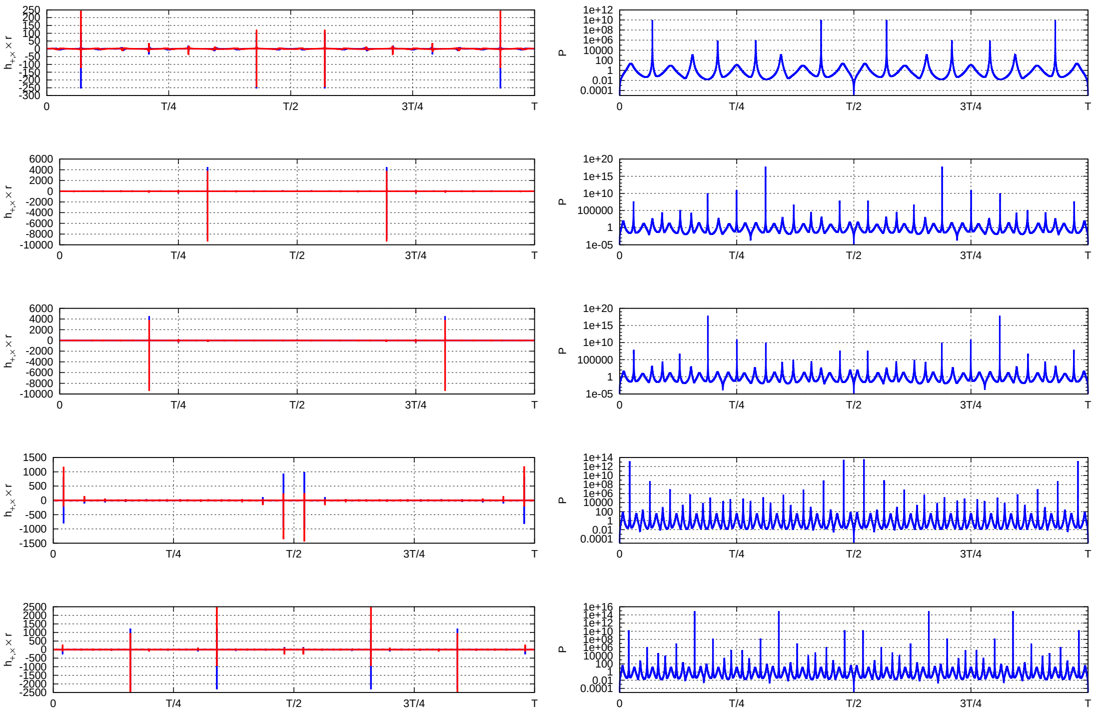

Figure 30: Same as in Figure 25 for orbits from the moth III sequence (Table 21). From top to bottom: IVc.5.A, IVc.12.A.α, IVc.12.A.β, IVc.17.A, IVc.19.A.

4.2.7 *Sequence V – figure-eight* (n, n)

Orbits from the figure-eight family have the lowest values of emitted power averaged over one period, see Figure 24. This is because they do not closely approach the two-body colision points (see their trajectories in shape-space, Figure 22).

Table 22: Orbits from sequence V – figure-eight. Columns are the same as in Table 16.

Name	$\dot{x}_1(0)$	$\dot{y}_1(0)$	λ	T	Θ(rad)	$\langle P \rangle$
V.1.A	0.216 343	0.332 029	2.574 29	26.128	0.245 57	1.4×10^0
V.1.B	0.211 139	0.333 568	2.583 87	26.127	0.277 32	1.4×10^0
V.4.A	0.403 776	0.327 021	1.908 49	104.394	-0.749 31	6.9×10^0
V.15.A	0.105 763	0.297 295	3.130 05	391.744	0.390 14	3.9×10^0
V.20.A	0.088 799	0.296 133	3.177 67	522.144	0.432 73	5.3×10^0

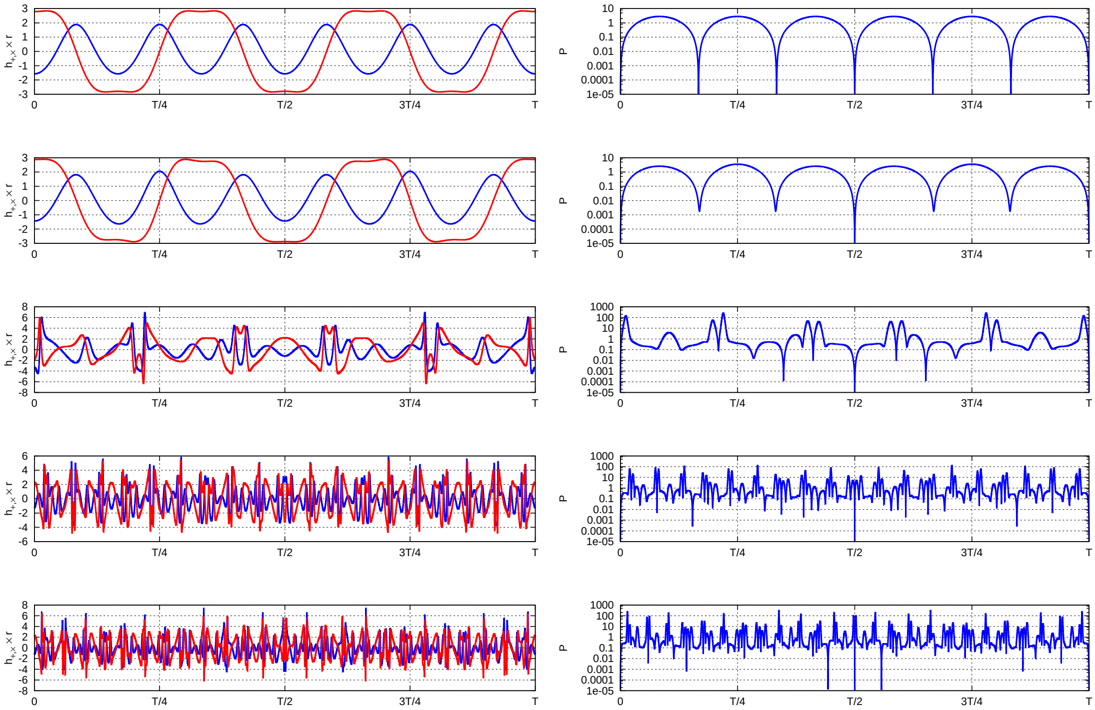

Figure 31: Same as in Figure 25 for orbits from the figure-eight sequence (Table 22). From top to bottom: V.1.A, V.1.B, V.4.A, V.15.A, V.20.A.

4.3 CONCLUSIONS

Periodic three-body orbits belonging to the same sequence of orbits have characteristic sequences of letters in their free group elements. Given the free group element it is in some cases possible to predict which of these sequences the orbit belongs to by recognizing these patterns. Orbits in the same sequence also have similarly looking trajectories, both in real space and the shape-space. Their waveforms and instantaneous power graphs also have similar appearances.

Several of the newly discovered orbits were explicitly predicted, and many more follow the trends described in Ref. [22]. Their (Kepler's third law) invariants $T|E|^{3/2}$ have linear dependence on the values of $(n+\bar{n})/2$, as was stated in the same reference. Several new orbits have an *odd* number of letters n, where previously only *even* numbers had been observed.

The new results suggest, however, that some of the sequences defined in Ref. [22] should be divided into subsequences, for example: the "moth I, II, III - butterfly III" sequence into at least three subsequences – starting from moth I, butterfly III and moth

III). Also, there are some indications that the goggles orbit should be excluded from the "butterfly I" sequence, as it has a completely different shape-space trajectory and its free group element does not fit into the overall pattern of that sequence. Perhaps it forms a sequence of its own with orbits that are yet to be discovered?

The luminosity of three-body periodic systems depends on the proximity of the closest approach to a two-body collision point, as can be seen by comparing their shape-sphere trajectories. The number of gravitational radiation bursts is also proportional to the number of these close aproaches.

All of the orbits have distinct gravitational waveforms. This means that if such gravitational wave signals were to be detected someday, it would be possible to tell from what kind of astronomical three-body system they originate.

Both waveforms and instantaneous emitted power graphs have reflectional symmetry about the midpoint $T/2$. In the case of orbits whose trajectories have two symmetry axes these graphs also have reflectional symmetry about $T/4$ within one half-period.

Some of these orbits have luminosities up to 13 orders-of-magnitude higher than comparable two-body systems; this suggests that they may lead to detectable gravitational radiation signals. Whether or not the gravitational waves from this kind of sources will be observable by contemporary or some future gravitational wave observatories depends on the absolute values of the masses, velocities and the average distances between the three celestial bodies involved. It also depends on the distribution of such sources in our Galaxy, which is currently unknown. The existence of such systems is connected to their stability, which has not been properly explored, as yet. Clearly, a number of theoretical tasks remain to be done before one can discuss realistic astrophysical scenarios in this regard. But, those are topics for someone else's theses.

5

APPENDICES

5.1 NUMERICAL METHODS

Unfortunately, the Runge-Kutta-Fehlberg method has one drawback – the energy of the system is not kept constant during the integration. Some other methods of integration, symplectic algorithms for example, do not exhibit energy drift, but such algorithms use fixed time step, so we would have to choose between low precision and long integration times. Energy drift in our computations varies widely from one solution to another and its order of magnitude ranges from $< 10^{-10}$ to $< 10^{-5}$.

5.1.1 *Initial conditions*

The masses of the three-bodies are chosen to be equal.[1] In our units, the gravitational constant G and the mass of each body m are set to 1. Results for different values of G and m can be obtained by scaling. Angular momentum L is set to zero.[2] The initial configuration of bodies is chosen to be:

$$\begin{aligned}
&x_1(0) = -1, \;\; x_2(0) = 0, \;\; x_3(0) = 1, \\
&y_1(0) = y_2(0) = y_3(0) = 0, \\
&\dot{x}_1(0) = \dot{x}_3(0) = p_1, \;\; \dot{x}_2(0) = -2p_1, \\
&\dot{y}_1(0) = \dot{y}_3(0) = p_2, \;\; \dot{y}_2(0) = -2p_2.
\end{aligned} \tag{18}$$

In this way, we are left with two-dimensional space of initial conditions parametrized by initial velocities p_1 and p_2.

5.1.2 *Search space*

First we have to choose if we want to search for absolutely or relatively periodic orbits, in which subset of initial conditions space we want to look for them, the maximal value of period T_0, and numerical precision ϵ - maximal numeric error per one integration step. For absolutely periodic ones we use return-proximity function eq. (4), and for relatively periodic function eq. (10). The relatively periodic function will also find absolutely periodic solutions, since every absolutely periodic solution is also a relatively periodic one. Orbits with vanishing angular momentum can be only absolutely periodic.

1 This method of numerical search that follows can easily be modified for systems with different mass ratios.

2 Further solutions belonging to the same family can be obtained by varying the value of L and mass ratios $\frac{m_1}{m_2}$ and $\frac{m_1}{m_3}$.

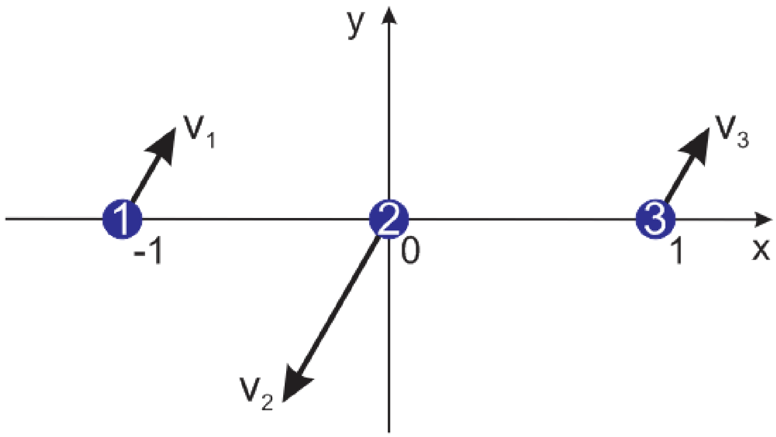

Figure 32: Initial configuration. $\mathbf{v}_1 = \mathbf{v}_3 = -\frac{1}{2}\mathbf{v}_2$

5.1.3 *Search method*

After we choose a "hunting ground" - an interval in the space of initial conditions $[p_{min,1}, p_{max,1}] \times [p_{min,2}, p_{max,2}]$, we create a grid of points with step s. For every grid point with initial conditions $\mathbf{X}_0$ we compute the value of the return-proximity function in the following way: distance from the initial condition is calculated by linear interpolation

$$d = \begin{cases} \|\mathbf{X}_0 - \mathbf{X}_i - a\,(\mathbf{X}_{i+1} - \mathbf{X}_i)\,\|, & a \in (0,1) \\ \|\mathbf{X}_0 - \mathbf{X}_i\|, & a \notin (0,1) \end{cases} \tag{19}$$

where

$$a = \frac{(\mathbf{X}_{i+1} - \mathbf{X}_i) \cdot (\mathbf{X}_0 - \mathbf{X}_i)}{\|\mathbf{X}_{i+1} - \mathbf{X}_i\|^2},$$

(see Figure 5.1.3) after every integration step from $\mathbf{X}_i$ to $\mathbf{X}_{i+1}$. The value of d will at first increase, when it starts to decrease it is checked whether it is minimal, and the minimal value of d and corresponding time T are stored – the resulting values are the return proximity function and corresponding period. Integration will stop after time reaches the maximal value of period T_0.

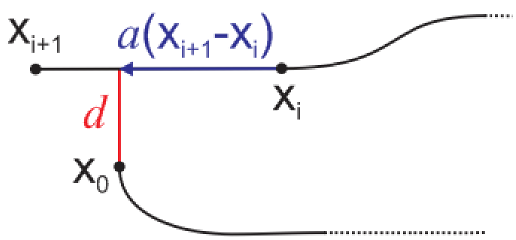

Figure 33: Linear interpolation. See eq. (19) for definitions of d and a.

5.1.4 *Plot of return proximity function*

Now we can plot the values of return proximity function for the whole hunting ground region. Local minima of this function are possible candidates for periodic solutions if they are less than some preset tolerance. Their initial velocities are calculated to the precision of step s. The next step is to apply the gradient descent method in order to increase this precision and to check if this is really a periodic solution.

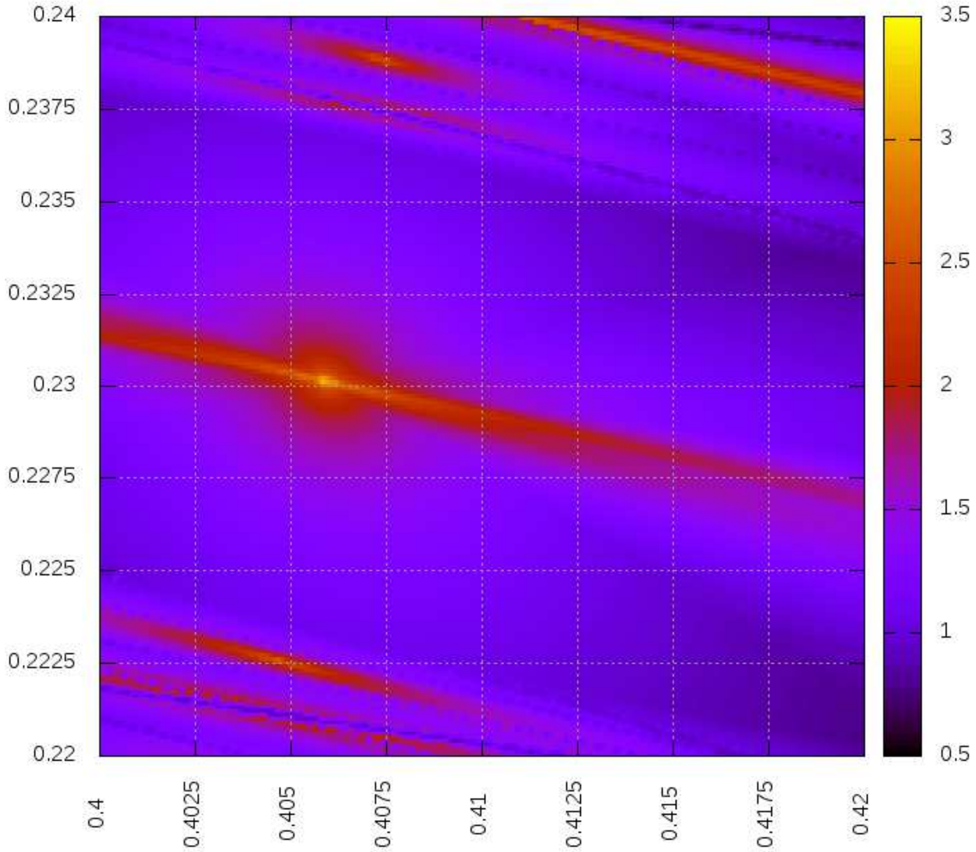

Figure 34: Example of a $-\log(d)$ graph in the region $[0.40, 0.42] \times [0.22, 0.24]$. Three canditate solutions are visible. The middle one is the previously known butterfly III orbit.

This method is not guaranteed to lead to every periodic orbit in the given range of initial conditions and period; it is possible that some solutions will be missed if the resolution is too low. Such orbits can be found with increased resolution.

5.1.5 *Gradient descent method*

The gradient descent method works as follows: a 5x5 grid with the initial grid resolution d_p is created around the candidate point and the return proximity function is calculated for each grid point; the candidate point is then moved to the grid point with minimal return proximity function, and the procedure is repeated with the grid resolution $d_p/2$. This procedure ends after the predetermined number of steps N_s, and the results are initial velocities with greater precision and a new return proximity function value which is always less than the starting one.

After the gradient descent method is applied, the new return proximity function is compared to some limit value, and all solutions with return proximity functions less than that value are considered to be periodic orbits of a three-body system. This limit value depends on the numerical precision of the integration method.

5.2 DERIVATION OF GRAVITATIONAL WAVES IN GENERAL RELATIVITY

This derivation closely follows Ref. [35].

In general relativity, the metric tensor $g_{\mu\nu}$ describes the curvature of space-time. Linearized theory is a weak field approximation of general relativity. In this case, the space-time is asymptotically flat – therefore we can divide the metric tensor into Minkowskian part $\eta_{\mu\nu} = \mathrm{diag}(-1, 1, 1, 1)$ and a small perturbation:

$$g_{\mu\nu} = \eta_{\mu\nu} + h_{\mu\nu}. \tag{20}$$

The name of this approximation stems from the fact that higher order terms of $h_{\mu\nu}$ are neglected – only the linear term is kept in expressions, unless it vanishes.

The linearized theory of general relativity can be thought of as a theory described by a symmetric, second-rank tensor field $h_{\mu\nu}$ that propagates in a Minkowski space-time. We can obtain the equations of motion by replacing eq. (20) into Einstein's equation in vacuum. After some straightforward computation we get:

$$\begin{aligned} G_{\mu\nu} &= R_{\mu\nu} - g_{\mu\nu}R = 0 \qquad (21)\\ &= \frac{1}{2}\left(\partial_\sigma\partial_\nu h^\sigma{}_\mu + \partial_\sigma\partial_\mu h^\sigma{}_\nu - \partial_\mu\partial_\nu h - \Box h_{\mu\nu} - \eta_{\mu\nu}\partial_\rho\partial_\sigma h^{\rho\sigma} + \eta_{\mu\nu}\Box h\right), \end{aligned}$$

where $\Box = -\partial_t^2 + \partial_x^2 + \partial_y^2 + \partial_z^2$ is the d'Alembertian in flat space and $h = \eta^{\mu\nu}h_{\mu\nu} = h^\mu{}_\mu$ is the trace of the perturbation.

Equation (20) can be written in a different coordinate system in such a manner that the $\eta_{\mu\nu}$ part is still a Minkowski metric tensor and the perturbation $h_{\mu\nu}$ is still small. It can be demonstrated (see Carroll ch.7.1, Ref. [35]) that the perturbations change according to the equation:

$$h^{(\epsilon)}_{\mu\nu} = h_{\mu\nu} + \epsilon(\partial_\mu\xi_\nu + \partial_\nu\xi_\mu), \tag{22}$$

where ϵ is a small parameter and ξ_{mu} is a vector field that generates a family of diffeomorphisms on the background space-time, in order for $h^{(\epsilon)}$ to represent the same physical situation as h. This equation is a gauge transformation in linearized theory. Alternatively, the parameter ϵ can be set to 1 and the vector field ξ_μ can be considered small. We can now choose a gauge and solve the Einstein equation. Just as in the case of electromagnetic waves, some gravitational wave gauges yield a clearer view of the underlying physics.

The perturbation tensor components can be divided according to their transformation properties under spatial rotations. The 00 component transforms as a scalar, the $0i$ components as a spatial three-vector w_i, and the ij components as a symmetric, second-rank spatial tensor. This spatial tensor can be further divided into a trace and a traceless part:

$$h_{ij} = 2s_{ij} + \frac{1}{3}h\delta_{ij} \qquad s_{ij} = \frac{1}{2}(h_{ij} - \frac{1}{3}h\delta_{ij}), \tag{23}$$

where $h = \delta^{ij}h_{ij}$ is the trace of h_{ij}. The traceless part s_{ij} is called the strain, and it turns out that it contains the only two propagating degrees-of-freedom in Einstein's equation - this is the part that describes the gravitational waves.

Out of many possible gauges, the transverse-traceless gauge is the most useful for dealing with gravitational waves. Transverse gauge fixes the strain and the three-vector perturbation to be transverse: $\partial_i s^{ij} = 0$ and $\partial_i w^i = 0$. This can be done by choosing the appropriate values of ξ^μ; ξ^i for s^{ij} and ξ^0 for w^i. In this gauge, Einstein's equation in vacuum becomes $\Box s_{ij} = 0$ – the wave equation. We use the vacuum form of the equation because we are now interested only in propagation of the waves; therefore we can solve the equation in a region far away from the source of gravitational waves.

If we wish to work with h_{ij} instead of s_{ij}, we can change to the transverse-traceless gauge, where all the other degrees-of-freedom except s_{ij} are set to zero. In this gauge, Einstein's equations in vacuum amount to:

$$\Box h^{TT}_{ij} = 0. \tag{24}$$

The new perturbation tensor

$$h^{TT}_{\mu\nu} = \begin{pmatrix} 0 & 0 & 0 & 0 \\ 0 & & & \\ 0 & & 2s_{ij} & \\ 0 & & & \end{pmatrix} \tag{25}$$

is a purely spatial, transverse and traceless symmetric two-index tensor:

$$h^{TT}_{0\mu} = 0 \qquad \partial_\mu h^{TT}_{\mu\nu} = 0 \qquad \eta^{\mu\nu}h^{TT}_{\mu\nu} = 0. \tag{26}$$

Now we can proceed to solve the equation (24). The general solution for the (free wave) D'Alembert equation is a plane wave: $h^{TT}_{ij} = \mathrm{Re}\left(C_{ij}e^{ik_\mu x^\mu}\right)$, where C_{ij} is a constant symmetric traceless and purely spatial two-index tensor:

$$C_{0\mu} = 0 \qquad \eta^{\mu\nu}C_{\mu\nu} = 0. \tag{27}$$

The wave vector k_μ is a constant null four-vector orthogonal to $C^{\mu\nu}$ (follows from eqs. (24) and (26)):

$$k_\mu k^\mu = 0 \qquad k_\mu C^\mu = 0. \tag{28}$$

The zeroth component of the wave four-vector is the frequency ω. We can choose a spatial coordinate system in such a way that the wave three-vector $\mathbf{k}$ is traveling in the $\mathbf{e}_z$ direction - then it has the form $k^\mu = (\omega, 0, 0, \omega)$. It follows from eqs. (27) and (28) that the only nonvanishing components of the $C_{\mu\nu}$ tensor are C_{11}, $C_{22} = -C_{11}$ and

$C_{12} = C_{21}$. The wave is completely characterized by these three numbers: ω, C_{11}, and C_{12}.

To see the effect of a passing gravitational wave on test particles we may use the geodesic deviation equation:

$$\frac{D^2}{d\tau^2} S^\mu = R^\mu{}_{\nu\rho\sigma} U^\nu U^\rho S^\sigma, \tag{29}$$

where τ is proper time, S^μ separation four-vector, U^μ four-velocity and $R^\mu{}_{\nu\rho\sigma}$ the Riemann curvature tensor. This equation describes the relative motion of nearby particles.

If the test particles are moving slowly, we can approximate the velocity four-vector with $U^\mu = (1, 0, 0, 0)$, since all corrections are of higher order in $h^{TT}_{\mu\nu}$. In this case we also have $\tau = x^0 = t$. After some calculations eq. (29) becomes

$$\frac{\partial^2}{dt^2} S^\mu = \frac{1}{2} S^\sigma \frac{\partial^2}{dt^2} h^{TT\mu}{}_\sigma. \tag{30}$$

This means that a gravitational wave affects test particles only in directions perpendicular to the direction of propagation. We can denote the two numbers which characterize the wave with: $h_+ = C_{11}$ and $h_\times = C_{12}$. Their meaning will soon become apparent.

We shall now analyze the effects of h_+ and $h_\times$ separately, by solving the equation (30) in two cases:

1. $h_\times = 0$:

$$\frac{\partial^2}{dt^2} S^1 = \frac{1}{2} S^1 \frac{\partial^2}{dt^2} \left(h_+ e^{ik_\sigma x^\sigma} \right) \tag{31}$$

$$\frac{\partial^2}{dt^2} S^2 = -\frac{1}{2} S^2 \frac{\partial^2}{dt^2} \left(h_+ e^{ik_\sigma x^\sigma} \right) \tag{32}$$

The solutions of this system of equations are:

$$S^1 = \left(1 + \frac{1}{2} h_+ e^{ik_\sigma x^\sigma} \right) S^1(0) \tag{33}$$

$$S^2 = \left(1 - \frac{1}{2} h_+ e^{ik_\sigma x^\sigma} \right) S^2(0). \tag{34}$$

This is the so-called "plus" polarization mode of a gravitational wave. Its name comes from the shape of the deformation a ring of test particles experiences under the influence of the wave, see Figure 5. Relative deformation is measured by the dimensionless strain h_+.

2. $h_+ = 0$:

$$\frac{\partial^2}{dt^2} S^1 = \frac{1}{2} S^2 \frac{\partial^2}{dt^2} \left(h_\times e^{ik_\sigma x^\sigma} \right) \tag{35}$$

$$\frac{\partial^2}{dt^2} S^2 = \frac{1}{2} S^1 \frac{\partial^2}{dt^2} \left(h_\times e^{ik_\sigma x^\sigma} \right) \tag{36}$$

The solutions of this system of equations are:

$$S^1 = S^1(0) + \frac{1}{2} h_+ e^{ik_\sigma x^\sigma} S^2(0) \tag{37}$$

$$S^2 = S^2(0) + \frac{1}{2} h_+ e^{ik_\sigma x^\sigma} S^1(0). \tag{38}$$

This is the "cross" mode of a gravitational wave. Again, its name comes from the shape of the deformation a ring of test particles experiences under the influence of the wave, see Figure 6, and $h_\times$ measures the relative deformation.

5.3 TABLE OF INITIAL CONDITIONS

Table 23: Initial velocities, periods and return proximity functions for all orbits in this thesis. Sequences of orbits are divided by horizontal lines.

Label	$\dot{x}_1(0)$	$\dot{y}_1(0)$	T	r.p.f.
I.2.A	0.306 893	0.125 507	6.236	$7.07 \cdot 10^{-7}$
I.2.B	0.392 955	0.097 579	7.004	$1.61 \cdot 10^{-6}$
I.5.A	0.411 293	0.260 755	20.749	$3.43 \cdot 10^{-7}$
I.8.A	0.412 103	0.283 384	34.248	$3.97 \cdot 10^{-7}$
I.12.A	0.408 211	0.243 685	48.487	$2.98 \cdot 10^{-7}$
II.4.A	0.080 584	0.588 836	21.271	$5.39 \cdot 10^{-7}$
II.6.A	0.186 238	0.578 714	33.641	$1.88 \cdot 10^{-6}$
II.8.A	0.144 812	0.542 898	38.062	$1.72 \cdot 10^{-6}$
II.11.A	0.184 279	0.587 188	63.535	$1.64 \cdot 10^{-6}$
III.3.A.α	0.513 938	0.304 736	17.328	$1.75 \cdot 10^{-6}$
III.3.A.β	0.282 699	0.327 209	10.963	$3.56 \cdot 10^{-6}$
III.9.A.α	0.513 150	0.289 437	50.408	$1.14 \cdot 10^{-6}$
III.9.A.β	0.276 237	0.331 714	32.841	$3.70 \cdot 10^{-7}$
III.12.A.α	0.416 822	0.330 333	55.790	$1.32 \cdot 10^{-6}$
III.12.A.β	0.417 343	0.313 100	54.208	$1.49 \cdot 10^{-6}$
III.15.A.α	0.414 396	0.339 223	70.493	$5.46 \cdot 10^{-7}$
III.15.A.β	0.417 701	0.303 455	66.752	$2.11 \cdot 10^{-6}$
IVa.2.A	0.464 445	0.396 060	14.894	$9.92 \cdot 10^{-7}$
IVa.4.A	0.439 166	0.452 968	28.670	$6.22 \cdot 10^{-7}$
IVa.6.A	0.429 090	0.475 313	42.830	$9.75 \cdot 10^{-8}$
IVa.8.A	0.401 574	0.490 047	54.087	$5.62 \cdot 10^{-7}$
IVa.8.B	0.396 528	0.492 290	53.746	$1.95 \cdot 10^{-5}$
IVa.8.C	0.405 043	0.492 281	55.039	$1.34 \cdot 10^{-6}$
IVb.3.A	0.405 916	0.230 163	13.866	$1.02 \cdot 10^{-7}$
IVb.11.A	0.395 637	0.154 450	41.789	$2.17 \cdot 10^{-7}$
IVb.15.A	0.395 205	0.142 197	55.820	$5.80 \cdot 10^{-5}$
IVb.19.A	0.393 934	0.134 728	69.740	$9.63 \cdot 10^{-7}$
IVb.24.A	0.350 112	0.079 339	79.476	$7.97 \cdot 10^{-6}$
IVc.5.A	0.383 444	0.377 364	25.840	$4.38 \cdot 10^{-7}$
IVc.12.A.α	0.463 804	0.357 385	68.645	$5.46 \cdot 10^{-5}$
IVc.12.A.β	0.429 325	0.373 739	64.874	$2.67 \cdot 10^{-6}$
IVc.17.A	0.413 909	0.344 900	82.863	$4.50 \cdot 10^{-4}$
IVc.19.A	0.403 994	0.366 295	93.786	$3.82 \cdot 10^{-6}$
V.1.A	0.347 113	0.532 727	6.325	$8.58 \cdot 10^{-7}$
V.1.B	0.339 393	0.536 191	6.290	$2.73 \cdot 10^{-6}$
V.4.A	0.557 809	0.451 774	39.594	$1.00 \cdot 10^{-6}$
V.15.A	0.187 116	0.525 972	70.742	$1.20 \cdot 10^{-6}$
V.20.A	0.158 293	0.527 887	92.178	$7.84 \cdot 10^{-6}$

6

REFERENCES

[1] V. Dmitrašinović, Milovan Šuvakov, and Ana Hudomal, Phys. Rev. Lett. 113, 101102 (2014)

[2] E.H. Bruns, Acta Math. **11**, 25 (1887).

[3] M. Tabor, *Chaos and Integrability in Nonlinear Dynamics - An Introduction*, John Wiley and Sons, New York (1988).

[4] J. L. Lagrange, Miscellanea Taurinensia **4**, 118 (1772); Oeuvres **2**, 67; Mécanique Analytique, 262; 2nd ed. **2**, 108; Oeuvres **12**, 101.

[5] R. Broucke and D. Boggs, Celest. Mech. **11**, 13 (1975).

[6] R. Broucke, Celest. Mech. **12**, 439 (1975).

[7] J.D. Hadjidemetriou, Celest. Mech. **12**, 155 (1975).

[8] J.D. Hadjidemetriou and Th. Christides, Celest. Mech. **12**, 175 (1975).

[9] J.D. Hadjidemetriou, Celest. Mech. **12**, 255 (1975).

[10] M. Henon, Celest. Mech. **13**, 267 (1976).

[11] M. Henon, Celest. Mech. **15**, 243 (1977).

[12] C. Moore, Phys. Rev. Lett. **70**, 3675 (1993).

[13] C. Simó, in *Celestial Mechanics*, edited by A. Chenciner, R. Cushman, C. Robinson, and Z. J. Xia (Am. Math. Soc., Providence, RI, 2002).

[14] Milovan Šuvakov and V. Dmitrašinović, Phys. Rev. Lett. **110**, 114301 (2013).

[15] M. Šuvakov, Celest. Mech. Dyn. Astron. **119**, 369 (2014).

[16] M. Šuvakov and V. Dmitrašinović, Am. J. Phys. **82**, 609 (2014).

[17] Carl Gustav Jacob Jacobi, (1884); reprinted by Chelsea Publishing Company, New York, (1969), pp. 221-231.

[18] R. Montgomery, Ergodic Theory and Dynamical Systems 27 (6), 1933-1946 (2007).

[19] R. Montgomery, Nonlinearity **11**, 363 - 376 (1998).

[20] Erwin Fehlberg, Computing (Arch. Elektron.Rechnen) 6, 61-71 (1970).

[21] M. Šuvakov, private communication (2013).

[22] V. Dmitrašinović and Milovan Šuvakov, Phys. Lett. A 379, 1939-1945 (2015).

[23] K. S. Thorne, arXiv:gr-qc/9506086v1.

[24] P. C. Peters and J. Mathews, Phys. Rev. **131**, 435 (1963).

[25] P. C. Peters, Phys. Rev. **136**, B1224 (1964).

[26] http://www.ligo.org/science/

[27] https://dcc.ligo.org/public/0014/T050174/001/PlaneMonDoc.pdf

[28] https://en.wikipedia.org/wiki/Gravitational-wave_astronomy

[29] M. Campanelli, C. O. Lousto, P. Marronetti, and Y. Zlochower, Phys. Rev. Lett. **96**, 111101 (2006).

[30] J. G. Baker, J. Centrella, D.-I. Choi, M. Koppitz, and J. van Meter, Phys. Rev. Lett. **96**, 111102 (2006).

[31] F. Pretorius, Phys. Rev. Lett. **95**, 121101 (2005).

[32] Y. Torigoe, K. Hattori, and H. Asada, Phys. Rev. Lett. **102**, 251101 (2009).

[33] T. Chiba, T. Imai, and H. Asada, Mon. Not. R. Astron. Soc. **377**, 269 (2007).

[34] H. Asada, Phys. Rev. D **80**, 064021 (2009).

[35] S. Carroll, *Spacetime and Geometry: An Introduction to General Relativity*, Addison Wesley, San Francisco (2004).